SYNTHESIS, SHORT RANGE ORDER STRUCTURE, AND THERMAL PROPERTIES OF MIXED OXY-SULFIDE NITRIDE (MOSN) GLASSES

Steven Kmiec, Steve W. Martin*

*Corresponding author

Email address: swmartin@iastate.edu

Department of Materials Science & Engineering

Iowa State University of Science & Technology

Ames, IA 50011

Abstract

Nitrogen doping has been shown to greatly improve the stability of solid electrolyte (SE) materials at the anode and cathode interfaces in all solid-state batteries (ASSBs) as widely demonstrated by the LiPON family of compositions. In an effort to expand the use of nitrogen in SEs, in this study, mixed oxy-sulfide nitride (MOSN) glasses were prepared by direct ammonolysis of the sodium oxy-sulfide phosphate Na₄P₂S_{7-x}O_x (NaPSO) glass series to understand the combined effects that oxygen and sulfur have on the incorporation of nitrogen. The short-range order (SRO) structures of the Na₄P₂S_{(7-x)-3/2y2}O_{x-3/2y(1-z)}N_y (NaPSON) glasses were investigated with Raman and infrared (IR) spectroscopies to understand the effect that nitrogen has in the glass structure. The N content of the glasses was quantified by elemental analysis and confirmed through weight change measurements. By combining this information, it was further possible to determine the anion

exchange ratio, z, for the N substitution of O and S as a function of the base NaPSO glass chemistry, x. The composition dependent glass transition temperature, $T_g(x)$, measured with differential scanning calorimetry (DSC), was found to correlate well with the measured N/P ratio, y, in the NaPSON glasses.

INTRODUCTION

Solid electrolytes (SEs) have received increased attention recently because they may enable development of all solid-state batteries (ASSBs) based in part upon sodium and lithium metal (SM/LM) anodes with energy densities exceeding that of current battery chemistries, such as Liion batteries (LIB)¹⁻⁴. Due to the complex requirements for the use of SM and LM anodes in ASSBs, a clear choice for a SE is still lacking⁵⁻⁷. Polymeric electrolytes have exhibited high conductivity, conformality, and processability; however, they are flammable and have poor conductivities at relatively low temperatures (<20°C)^{3, 8-10}. Some inorganic oxide materials such as sodium beta-alumina, NASICON, and LLZO are stable in contact with SM and LM and exhibit high ionic conductivities reaching > 10⁻⁴ S/cm at 25°C¹¹⁻¹³. Unfortunately, despite great advancements in the last 10 years, these polycrystalline oxide ceramics present many challenges when transitioning synthesis and production beyond a laboratory scale^{13, 14}. Sulfide materials have also emerged as viable candidates for SEs due to their high ionic conductivities and low-energy synthesis¹⁵⁻¹⁷. Nevertheless, sulfide materials are widely known to be highly reactive with other compounds, leading to challenges with processing and performance¹⁸⁻²⁰.

Glassy SEs (GSEs) are a promising alternative to polycrystalline ceramic electrolytes as they are highly conductive, fully dense and resistant to dendrite growth, and capable of being drawn or sputtered as thin films^{13, 21-25}. Dudney *et al.*^{26, 27}, demonstrated these properties in the

well-known lithium oxy-nitride glass, LiPON, which is highly resistant to dendrites and chemically stable in contact with LM and high voltage transition metal cathodes. Unfortunately, LiPON is limited to use in thin-film batteries due to its relatively low ionic conductivity of ~ 1 x 10^{-6} S/cm at 25° C²⁸. More recently, our research group has extensively examined invert mixed oxy-sulfide (MOS) glasses in an effort to blend the properties of oxide and sulfide GSEs to optimize both the ionic conductivity and the electrochemical stability^{29, 30}. Here, as is commonly used, an invert glass composition has an alkali (or alkaline earth) cation ratio to total glass former cation, such as P, greater than 1. These invert glasses are most often studied as GSEs because the alkali cation conductivity is often, but not always, a strong and positive function of the alkali to glass former ratio^{31, 32}.

In conjunction with the work by Mascaraque *et al.*³³, this paper focuses on the first mixed oxy-sulfide nitride (MOSN) glasses prepared via direct ammonolysis of oxy-sulfide melts, as a new class of GSEs for potential use as SEs. The Na₄P₂S_{7-x}O_x (NaPSO) glass system was chosen as the base compositions to understand the effect ammonolysis has on MOS invert glasses containing considerably higher concentrations of alkali modifier than traditional melt quenched glasses. In previous reports on these MOS GSEs, their preparation, short range order (SRO) structures and thermal properties have been studied.

The nitrogen solubility is a function of the Na concentration, the O to S ratio in the MOS glass, the glass forming cation, here P, and the type of structural site that the nitrogen enters into the GSE structure. The theoretical maximum N/P ratio limit is 1.67 for phosphorus tetrahedrally coordinated to nitrogen (PN₄) in the compound P₃N₅³⁴⁻³⁶. Within this nitride compound, two nitrogen species are observed; tri-coordinated nitrogen (N_t) bonded to three different P centers, and linearly coordinated nitrogen (N_d) bonded through a double bond to one P and a single bond

to a second P center³⁶⁻³⁹. Other compounds exist with greater concentrations of nitrogen but rely heavily on ionic bonding with alkali or alkaline earth metals such as Li₃N and Ca₃N₅^{39, 40}. These structural units are not favorable for glass formation or chemical stability as they readily react with O_2 and H_2O .

The increased chemical stability of N-doped oxide and oxy-sulfide glasses can be attributed to the P-N-P bonds that are formed in place of bridging oxygen (BO) P-O-P bonds, which prevent or dramatically slow oxidation, hydrolysis, and electrochemical reduction and oxidation below the glass transition temperature (Tg), when in contact with oxygen (air), water, alkali metal, and high voltage cathodes^{38, 39, 41}. Munoz *et al.* ^{42, 43}, observed that lithium phosphorus oxide (LiPO) glasses demonstrate improved nitrogen absorption with increasing modifier concentration, reaching the highest nitrogen concentration in the 0.6Li₂O + 0.4 P₂O₅ composition. These authors reported that further additions of Li₂O, however, severely decreased the number of BOs in the LiPO GSEs and thereby greatly reduced the number of available sites for nitrogen to occupy and, consequently, reduced the uptake of nitrogen. Simultaneously, the viscosity and liquidus temperature of the melt increased which, in turn, decreased the rate of N incorporation and the thermal stability of the formed P-N bonds^{44, 45}.

In the invert glasses studied here, the combined fractions of BOs and bridging sulfurs (BSs) is small, nominally 1/7, compared to the combined fractions of non-bridging oxygens (NBOs) and non-bridging sulfurs (NBSs), nominally 6/7. It is the purpose of the current work here, therefore, to understand the effects of nitrogen substitution on the highly modified the Na₄P₂S_{7-x}O_x MOS glass series.

In this study, it has been found that the distribution of SRO structures present in the base MOS glasses directly determines the type, N_t and N_d , of nitrogen incorporated. The different

nitrogen containing SRO species have been found to produce different intermediate range order (IRO) structures, which generate large changes in the physical properties such as the T_g reported here. In future papers in this series, the effects of N on the ionic conductivity and the electrochemical performance of these MOSN GSEs will be reported.

Experimental methods

Sample Preparation

Annealed bars of the MOS glass compositions were prepared from 4-5g batches following methods described by Kmiec *et al.*³⁰ in a N₂ glovebox using as received sodium sulfide (Na₂S 99.9% Alfa Aesar), phosphorus pentasulfide (P₂S₅, 99.95% Sigma Aldrich), and phosphorus pentoxide (P₂O₅, 99.95% Fisher Scientific). All samples were melted at temperatures between 500-580°C for 15min, and then were cast into a preheated mold set to ~35°C below the T_g , and annealed for ~3 hours then cooled to room temperature at a rate of 1°C/min. All samples were stored in a N₂ glovebox to prevent reactions with H₂O and O₂, until being subjected to the ammonolysis process and further testing.

Ammonolysis of Na₄P₂S_{7-x}O_x glasses

Ammonolysis of the Na₄P₂S_{7-x}O_x glasses follows the methods used by De Souza *et al.*⁴⁶, for the production of LiPON and NaPON bulk glasses. Due to the mass dependence on the N uptake into the melt, the sample size was held between 2.5g and 3.5g for all experiments by controlling the geometry of the glass bars⁴⁶. The ammonolysis system is depicted in Fig. S1 and is

comprised of a mullite tube furnace equipped with two water cooled end caps for N_2 and NH_3 gas inflow and exhaust. The exhaust port cap was equipped with a pushrod to move the sample during the experiment without atmospheric contamination. This allowed the untreated glass bars to be moved into the hot ammonolysis zone of the furnace and, after ammonolysis, the NH_3 treated melts to be moved out of the hot zone of the furnace into the cold zone outside of the furnace. This feature allowed the time and temperature of the ammonolysis to be carefully controlled and allowed the un-nitrided composition to cool more quickly such that wider compositional ranges of glass formation could be observed. Otherwise, the slow heating and cooling, << 1°C/min, of the large tube furnace would lead to relatively uncontrolled time and temperatures of ammonolysis and often cause crystallization of the melts.

The NaPSO MOS glass bars were transferred from a N₂ glovebox in an airtight container to the cold zone (~30°C) of the nitrogen filled tube furnace that had been pre-heated to the ammonolysis temperature of 520°C. This temperature was observed to be the best compromise such that the melt was fluid enough for diffusion and the subsequent reaction of the NH₃ throughout the MOS melt, but not so high that thermal decomposition and loss of the incorporated N would result. The furnace was then sealed and purged for ~10 min with N₂ gas at a rate of 25 ml/min. Once the tube was purged with nitrogen, the sample was pushed into the hot zone in the furnace, replicating the melting conditions of the base glass samples reported by Kmiec *et al* ³⁰. Immediately after moving the sample to the hot zone, the gas flow was switched from N₂ to NH₃. All samples were processed under NH₃ for incremental amounts of time, 0.5, 1, 2, 3, 6 h, using a constant furnace temperature of 520°C and NH₃ flow rate of 150 ml/min. Once the ammonolysis time was reached, the gas flow was switched back to N₂, the furnace was turned off, and the sample was pushed out of the hot zone to increase the cooling rate to ~5°C/min to promote glass formation

as described above. Once cooled, the sample was removed from the ammonolysis furnace and transported back to the N_2 glovebox for characterization.

Nitrogen Analysis (N/P Determination)

Weight Change Measurements

The mass of each glass sample was measured before (m_i) and after (m_f) each ammonolysis procedure using a Sartorius QUINTIX213-1S (± 0.001 g) precision balance. Because there was negligible weight loss during comparable processing at comparable temperatures without NH₃ gas, all weight loss could be assumed to be due to the incorporation of nitrogen. From these measurements the weight change fraction (WCF) was calculated using Eq. 1 to model the progress of ammonolysis reaction.

Wt. Change Fraction_(Expt.)
$$\equiv WCF_{(Expt.)} = \left(\frac{m_f - m_i}{m_i}\right)$$
 Eq. 1

CHNS Combustion Analysis

Elemental analysis was performed using a Thermo FlashSmart 2000 CHNS Combustion Elemental Analyzer, calibrated with a cysteine standard, to determine the concentration of nitrogen in the nitrided glasses. All samples were run in triplicate, prepared with V₂O₅ to ensure statistical relevance, with a combustion and reduction temperature of 975°C. The atomic mass fraction nitrogen (MFN) for each of the measured samples was then used to experimentally determine the glass composition and resulting N/P ratio for MOSN samples, see below.

Differential Scanning Calorimetry (DSC)

Thermal characterization was performed using a Perkin-Elmer Pyris 1 DSC calibrated with indium and tin standards. Experiments were conducted on bulk pieces of glass packed into hermetically sealed aluminum pans inside a nitrogen glove box. Baseline scans were run before each experiment using empty sample pans. All experiments were conducted under 25 ml/min nitrogen gas flow, and samples were heated at 20°C/min from 25°C to 450°C to identify the glass transition (T_g), crystallization (T_c), and melting (T_m) temperatures A new sample was then packed and thermally cycled in triplicate at +20°C/min and -20°C/min in the DSC from well below T_g to below T_c to the determine the T_g of the glass. Values for T_g were calculated using the onset method.

Raman Spectroscopy

Raman spectra were collected with an inVia 488 nm Renishaw Coherent Laser calibrated using an internal silicon reference standard centered to 520 cm⁻¹ (± 0.5). Bulk glass samples were measured in a sealed sample holder under N_2 to prevent oxygen and water contamination during measurement. Each sample was measured from 100 cm⁻¹ to 2500 cm⁻¹ using a 20x objective, a collection time of 15 seconds per accumulation, at least 10 accumulations at 12 mW power, and a spot size of $\sim 50~\mu m^2$. Multiple measurements were taken across the sample surface to determine compositional and structural homogeneity. In all cases, nearly identical spectra were collected independent of the beam location.

FT-IR Spectroscopy

A Bruker IFS 66v/s FT-IR spectrometer was used to collect the mid-IR (MIR) spectra. Samples were prepared by mixing ~2 wt.% of the glass with ~98 wt.% dry CsI using a mortar and pestle and then cold pressed to form a thin, optically translucent pellet. MIR spectra were collected from 400 cm⁻¹ to 4000 cm⁻¹ using a potassium bromide (KBr) beam splitter. All measurements were performed under vacuum using 4 cm⁻¹ resolution and 32 accumulations. Samples were transferred from the glove box to the FT-IR spectrometer in a sealed container and stored in a small glove box attached to the top of the FT-IR spectrometer kept under constant N₂ flow to prevent contamination.

Results

Nitrogen Determination

Weight Loss Measurements

The weight of each sample was measured before and after the ammonolysis process and the WCF is given as a function processing time for each base composition in Fig. 1. All of the samples tested lost weight upon ammonolysis and this is consistent with the expected mole ratio change of 1 N/1.5 O and 1 N/1.5 S. As Fig. 1 shows, all the WCF values for all samples exhibited a non-linear decrease in weight with processing times and reached a limiting value, the higher the oxygen content in the glass, higher *x*, the larger the WCF value. All of the WCF values are reported in Table S1. The Na₄P₂S₇ glass exhibited the smallest limiting WCF value under the fixed processing temperature of 520 °C used here, showing a -0.039 change after 6 h of ammonolysis. A systematic increase in the magnitude of the limiting WCF value is observed with increasing

amounts of oxygen, reaching a maximum magnitude of \sim -0.13 for the x=3 NaPSO glass. The Na₄P₂S₆O and Na₄P₂S₅O₂ glasses achieved a maximum WCF of -0.083 after 6 h of ammonolysis at 520°C. The initial slope, proportional to the rate of N incorporation, of the weight loss curves is observed to increase with x.

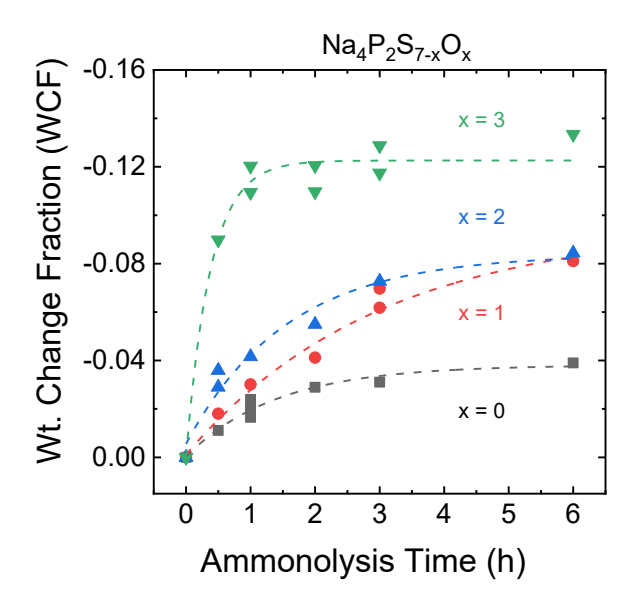


Figure 1. Measured weight loss from the ammonolysis of 5g bars of various Na₄P₂S_{7-x}O_x glasses as a function of processing time. Larger weight losses are observed in samples that contained greater concentrations of oxygen. Lines act as a guide to the eye.

CHNS Measurements

CHNS combustion analysis was used to determine the MFN values for all of the glass samples for the 6 h ammonolysis. For the Na₄P₂S₅O₂ sample, it was also used to determine the MFN for all of the ammonolysis treatments. The MFN values are given in Table S1 and plotted in Fig. 2 as a function of ammonolysis time. Similar to the WCF, the MFN values increase with ammonolysis and for the Na₄P₂S₅O₂ reaches a limiting maximum value at 6 h. We assume for the purposes here that since the WCF and MFN values are highly correlated, Table S1, and because

Fig. 2 shows that the WCF values for the $Na_4P_2S_5O_2$ composition also appear to reach a limiting asymptotic value at 6 h, the MFN value measured for the x = 0, 1, and 3 glasses at 6 hrs. also represent the limiting maximum values for the incorporation of N under the ammonolysis conditions used here.

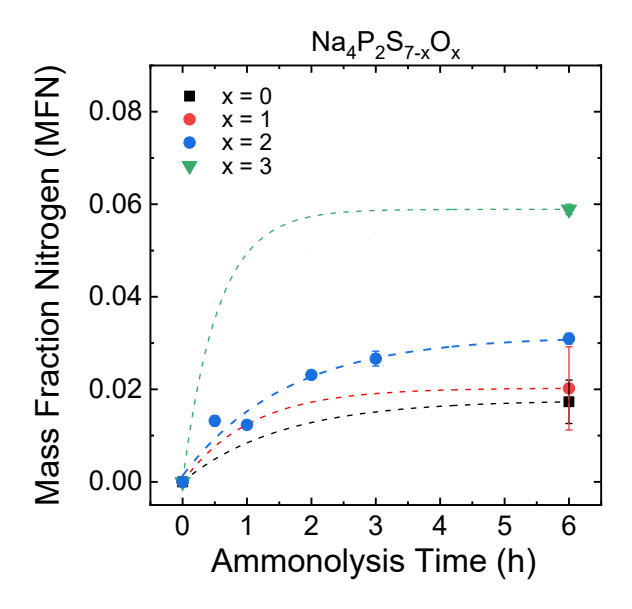


Figure 2. Compositional analysis of nitrogen for the Na₄P₂S₅O₂ + N series determined via CHNS measurements reported in weight percent. Dotted lines are guides to the eye only, based on inferences from the WCF shown in Fig. 1.

Table 1. Tabulated weight change fraction (WCF) and mass fraction nitrogen (MFN) values for the Na₄P₂S_{7-x}O_x glasses processed under direct NH₃ flow for variable amounts of time at 520°C.

		Ammonolysis Time (h)						
Sample	Calc. Parameter	0.5	1	2	3	6		
Na ₄ P ₂ S ₇	N/P Ratio	0.07	0.12	0.17	0.18	0.23		
	WCF	-0.0114	-0.0202	-0.0288	-0.0314	-0.0391		
	MFN	0.0049	0.0087	0.0126	0.0138	0.0173		
Na ₄ P ₂ S ₆ O	N/P Ratio	0.09	0.155	0.215	0.345	0.375		
	WCF	-0.0176	-0.0301	-0.0415	-0.0658	-0.0713		
	MFN	0.0071	0.0123	0.0173	0.0285	0.0312		

Na ₄ P ₂ S ₅ O ₂	N/P Ratio	0.16	0.18	0.27	0.34	0.38
	WCF	-0.0291	-0.0373	-0.0550	-0.0713	-0.0794
	MFN	0.0133	0.0134	0.0230	0.0295	0.0332
Na ₄ P ₂ S ₄ O ₃	N/P Ratio	0.41	0.53	0.53	0.57	0.62
	WCF	-0.0896	-0.1146	-0.1147	-0.1228	-0.1330
	MFN	0.0373	0.0497	0.0498	0.0539	0.0594

Differential Scanning Calorimetry (DSC)

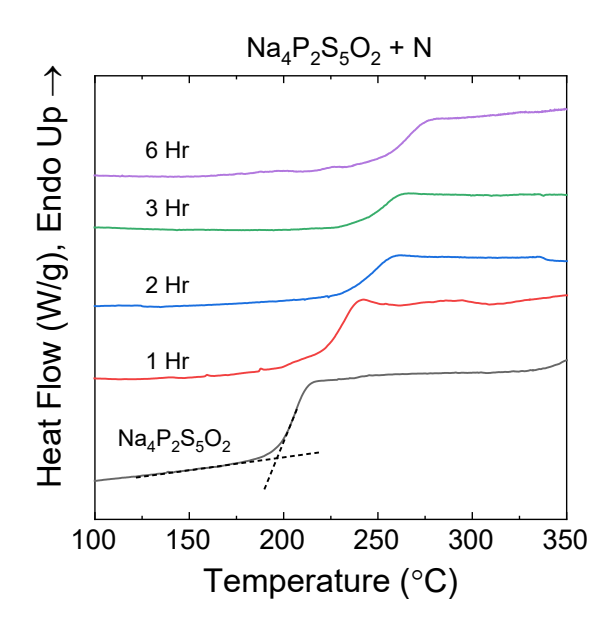


Figure 3. Example DSC Thermograms of the Na₄P₂S₅O₂+N glass series measured with a heating rate of 20°C/min, highlighting the effect ammonolysis time has on the glass transition temperature (T_g).

The thermal properties of the NaPSON glasses were measured using DSC to determine the T_g of the MOSN glasses. Thermograms of the Na₄P₂S₅O₂ + N glasses are shown in Fig. 3. A T_g = 190°C was measured in the Na₄P₂S₅O₂ base glass that increased by ΔT_g = 62°C after 6 h of ammonolysis. The increasing T_g is shown to be non-linear as seen in Fig. 4; exhibiting the largest change after the first hour, and approaching a plateau at longer processing times. The composition dependent T_g as a function of nitridation time exhibits a trend similar to the WCF reported in Fig.

1. The Na₄P₂S₄O₃ series displayed the most significant increases in T_g , showing $\Delta T_g = 85$ °C after 1 h and $\Delta T_g = 120$ °C after 6 h. The pure sulfide sample exhibited the smallest change in T_g , increasing by only 20°C, even after ammonolysis times up to 6 h. The MOS glasses, $1 \le x \le 3$, exhibited much larger changes under these same conditions, with T_g 's increasing by ~100°C in the Na₄P₂S₄O₃ composition.

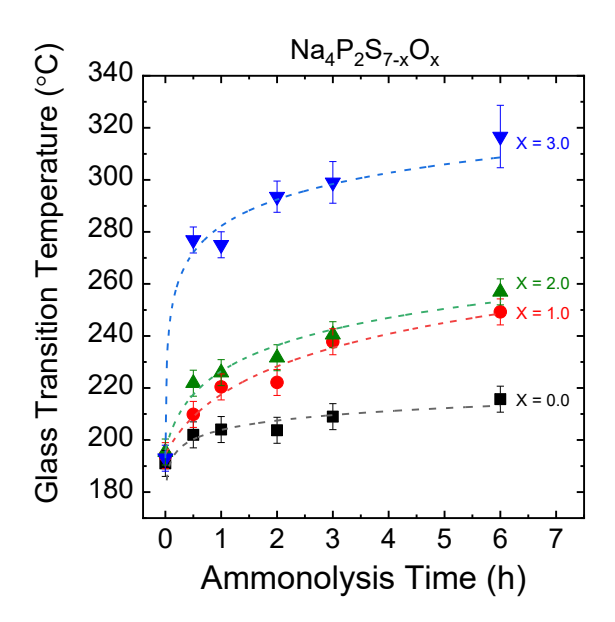


Figure 4: Measured T_g 's from the ammonolysis of 3-5g bars of various Na₄P₂S_{7-x}O_x glasses as a function of ammonolysis time. Samples that contained greater concentrations of oxygen exhibited larger changes in the T_g .

Raman Spectroscopy

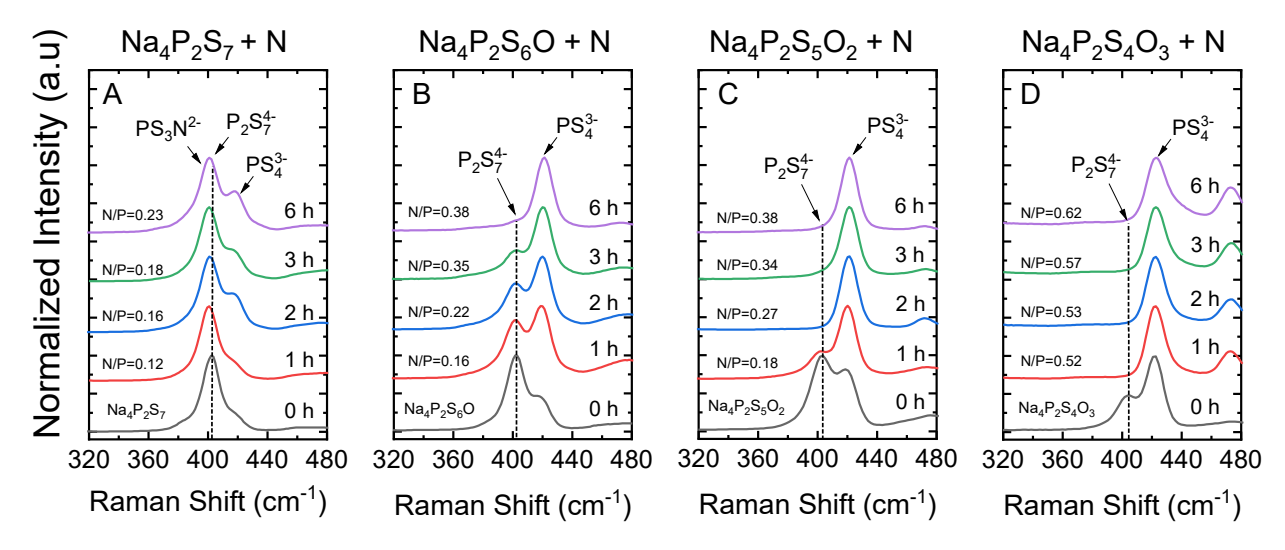


Figure 5. Raman spectral evolution of a) Na₄P₂S₇ +N, b) Na₄P₂S₆O+N, c) Na₄P₂S₅O₂+N, d) Na₄P₂S₄O₃+N, glasses directly nitrided for 0-6 h.

The Raman spectra of the Na₄P₂S₇ + N GSEs are given in Fig. 5a over the 320 to 480 cm⁻¹ spectra range, where all of the dominant spectra modes are observed, and show a systematic change in the SRO structures of the NaPSON GSEs with ammonolysis time. The most prominent band in the base sulfide glass is centered at 403 cm⁻¹ and has been assigned to the $v(PS_3)$ of NBS in the P₂S₇⁴⁻ (P^{1(S)}) anion^{18, 47, 48}. With increasing N/P ratios, this band shifts to lower frequencies reaching a peak position of 398 cm⁻¹ in the 6 h sample, suggesting the presence of new P^{1N} SRO units. The shoulder centered at 418 cm⁻¹ grows in intensity with nitrogen incorporation and has been assigned to the $v(PS_3)$ of NBS in the PS₄³⁻ anion^{48, 49}. The evolution of this band suggests the ammonolysis of the P₂S₇⁴⁻ anion produces non-networking P⁰ species as a product.

The Raman spectra of the $Na_4P_2S_6O + N$ GSEs are given in Fig. 5b, revealing a similar trend to the pure sulfide glass, where P^0 species are formed with longer processing times. In the base glass, the bands centered at 403 cm⁻¹ and 418 cm⁻¹ are still assigned to the $\nu(PS_3)$ of NBS in

 $P_2S_7^{4-}$ and PS_4^{3-} (P^0) anions, respectively, where the superscript refers to the numbers of BSs. With increasing nitrogen content, increasing N/P ratios, the mode assigned to $P^{1(S)}$ units, at 403 cm⁻¹, is consumed as a result the ammonolysis reaction and is replaced by the mode assigned to P^0 species at 418 cm⁻¹.

The effects of nitrogen incorporation in the Na₄P₂S₅O₂ and Na₄P₂S₄O₃ can be seen in the Raman spectra given in Figs. 5c-d, respectively. In both series, the intensity of the mode assigned to the P^{1(S)} species decreases rapidly after only two hours of ammonolysis and are not visible in samples with higher N/P ratios. As a result, the dominant band in the MOSN glasses is centered at ~420 cm⁻¹ and has been assigned to the NBS of P⁰ species. Additional information on the Raman spectra in these glasses, showing a wider spectral range, is provided in Fig. S2.

MIR Spectroscopy

P₃N₅

As a model compound for the P-N bonding in these NaPOSN GSEs, the MIR spectra of P_3N_5 was investigated to isolate the MIR bands associated with the P-N bonds. P_3N_5 contains both N_t and N_d species which are both IR active. The spectra published in literature reveals three distinct envelopes in the MIR region. The first envelope spans from 400 cm⁻¹ to 750 cm⁻¹ and contains several sharp modes centered at 495, 625, 673, and 710 cm⁻¹ which have been assigned to the network bending $\delta(P-N)$ modes^{39, 40, 50}. The second envelope spans from 750 cm⁻¹ to 1100 cm⁻¹ and contains the stretching modes of the $P-N_t$ configurations. Three unique modes emerge within this envelope with the most dominant band centered at 913 cm⁻¹ and the less prominent modes centered at 856 cm⁻¹ and 974 cm⁻¹, which have not been specifically identified in literature. The

final envelope spans from 1100 cm⁻¹ to 1500 cm⁻¹ and contains the stretching modes of the P-N_d configurations. The most intense mode in this envelope is centered at 1410 cm⁻¹, combined with two shoulders centered at 1279 cm⁻¹ and 1348 cm⁻¹, all of which arise from a distribution of nitrogen species in the PN₄ tetrahedra.

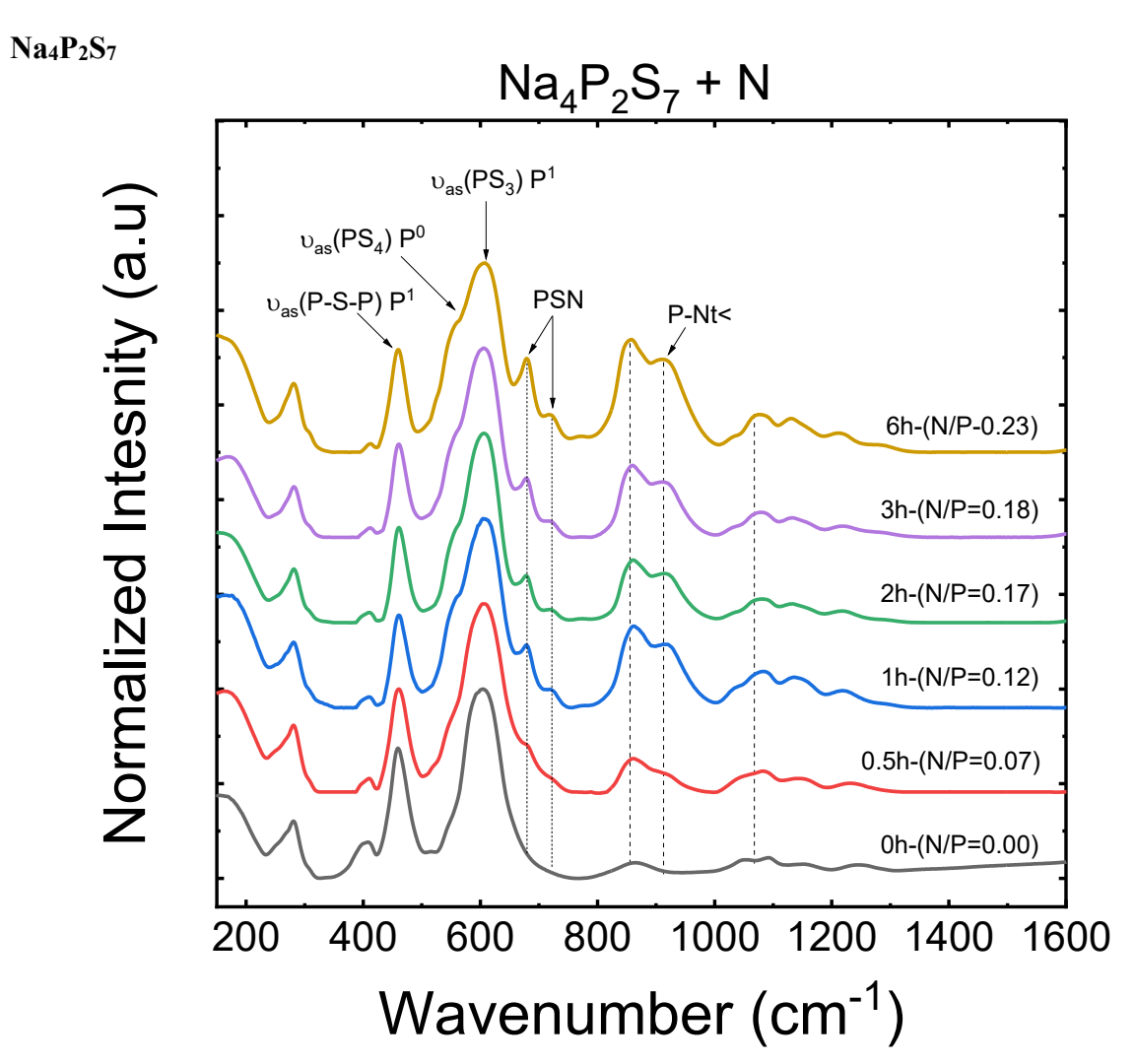


Figure 6. MIR spectra of Na₄P₂S₇ glass directly nitrided for 0-6 h.

The MIR spectra of $Na_4P_2S_7$ is shown in Fig. 6. Upon nitrogen incorporation, the $\delta(P-S)$ and $\nu(P-S)$ modes of the P^0 anion, centered at 280 cm⁻¹ and 560 cm⁻¹, respectively, increase becoming more prominent in the $Na_4P_2S_7$ 6 h sample. The sharp band centered at 460 cm⁻¹,

assigned to the $v_{as}(P-S-P)$ of the P_2S_7 anion, decreases slightly with the addition of nitrogen. The mode centered at 680 cm⁻¹ is consistent with the $\delta(P-N)$ mode in the P_3N_5 spectra centered at 671 cm⁻¹. The second mode at 720 cm⁻¹ is assigned to the bending $\delta(P-N_d)$, which is consistent with the shorter P=N bond and higher resonant frequencies⁴⁰. The two modes centered at 858 cm⁻¹ and 910 cm⁻¹ are assigned to tetrahedra possessing at least one N_t species and are notable compared to the other modes in the series³⁹.

Na₄P₂S₆O

The MIR spectra of Na₄P₂S₆O + N glasses are given in Fig. S3 and reveal significant structural changes with ammonolysis times. With the incorporation of nitrogen, the $v_{as}(P-S^-)$ of the P₂S₇⁴⁻ anion, centered at 605 cm⁻¹, shifts to higher frequencies while decreasing in intensity. After 6 h of ammonolysis, this mode has been partially replaced by the $v_{as}(P-S^-)$ of the P⁰ species to become shoulder centered at 615 cm⁻¹. Unlike the $v_{as}(P-S^-)$ of the P^{1(S)} species, the sharp mode centered at ~460 cm⁻¹, assigned to the BS $v_{as}(P-S-P)$ mode in P^{1(S)} anion, disappears entirely with the addition of nitrogen, as shown in Fig. S3. Accompanying the observed structural shift, is the emergence of modes between 600 cm⁻¹ and 800 cm⁻¹ that are associated with $\delta(P-N)$ modes. Similar to the Na₄P₂S₇ + N series, $\delta(P-N_t)$ and $\delta(P-N_d)$ modes appear at 680 cm⁻¹ and 720 cm⁻¹, respectively. Another mode grows in this region, centered at 667 cm⁻¹, which is attributed to the $\delta(P-N_t)$ of PX₂N₂ [X = O,S] tetrahedra. The mode with the highest frequency in this region is centered 784 cm⁻¹ and is very weak relative to the rest of the spectra which will tentatively be assigned to the $\delta(P-N_d)$ mode of a PS_{4-x}N_x tetrahedra.

Na₄P₂S₅O₂

Upon ammonolysis, the MIR modes, Fig. S4, associated with $P^{1(S)}$ species, $v_{as}(P-S-P)$ at 460 cm⁻¹ and $v_{as}(PS_3)$ at 630 cm⁻¹, are replaced by the mode at 580 cm⁻¹, which grows in intensity to become a dominant mode in the $Na_4P_2S_5O_2$ 6 h sample. The $v_{as}(P-O-P)$ modes of $P^{2(O)}$ and $P^{1(O)}$ SRO species are fairly broad and positioned at 874 cm⁻¹ and 945 cm⁻¹, respectively³⁰. An additional mode centered at 1150 cm⁻¹, assigned to v_{as} (O-P-O) / NBO of $P^{2(O)}$ species, increases in intensity relative to the surrounding NBO peaks reaching a maximum after six hours. The O-P-O bands convolute to from a mound by the formation of stretching of the P-N modes in the 6 h sample. Lastly, the broad shoulder that forms beyond 1300 cm⁻¹ has been assigned to the P-N_d bond.

Na₄P₂S₄O₃

The effect of ammonolysis is apparent in the MIR spectra of the Na₄P₂S₄O₃ glasses which are given in Fig. 7. The mode, centered at 617 cm⁻¹ and assigned to the NBS of the P¹ species, decreases with nitrogen incorporation and is replaced by the mode centered at the NBS of P⁰ tetrahedra. The modes assigned to BOs, between 600 cm⁻¹ and 800 cm⁻¹, were found to disappear with the incorporation of nitrogen. The v_{as}(P-O-P) mode of P^{2(O)} species is observed in the base glass at 890 cm⁻¹ which decreases with increased ammonolysis times while shifting to higher frequencies. The mode observed at 905 cm⁻¹ is in good agreement with v(P-N_t) modes for crystalline P₃N₅³⁹. The broad v_{as}(P-O-P) mode of the P^{1(O)} species, centered at 964 cm⁻¹ in the base glass, splits into two new modes at 990 cm⁻¹ and 950 cm⁻¹ which are assigned to the v(P-N_t) and v_{as}(P-O-P) modes, respectively. In the oxide O-P-O envelope, ranging from 1000 cm⁻¹ to 1400 cm⁻¹, the bands at 1050, 1100, and 1163 cm⁻¹ have been assigned to the NBOs of the P⁰, P¹, P² oxide species. A shoulder grows in at 1100 cm⁻¹, which is associated with the v_{as}(O-P-O) mode of P^{1(O)}

or $P^{1(N)}$ SRO species. Lastly, the $v_{as}(P=O)$ mode at 1250 cm⁻¹ broadens with the incorporation of nitrogen and is attributed to the formation of $v_{as}(P-N_d)$ species^{39,51}.

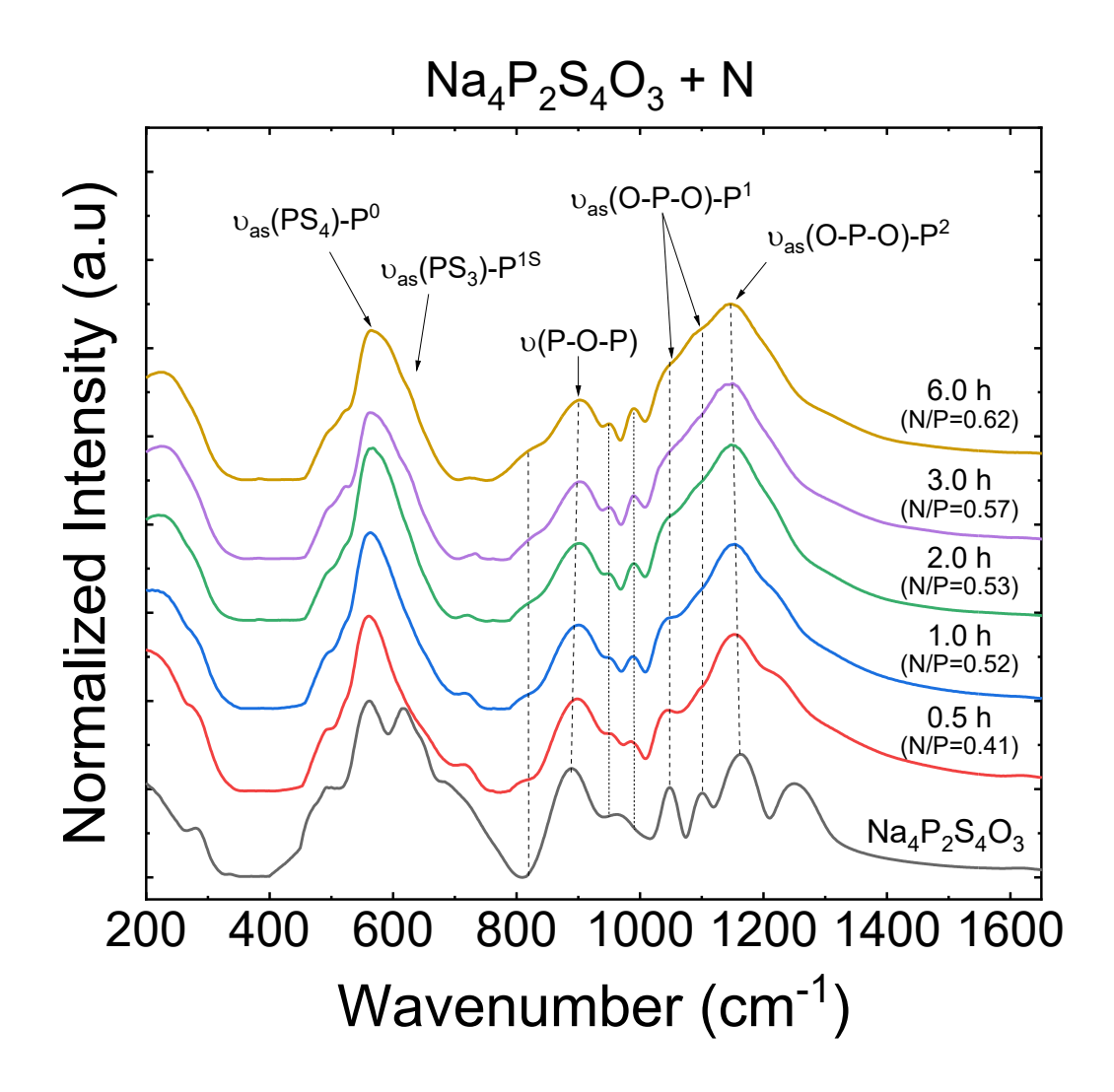


Figure 7. MIR spectra of Na₄P₂S₄O₃ glass directly nitrided for 0-6 h.

Discussion

Nitrogen Analysis (N/P determination)

Alkali Meta-Phosphate Oxy-Nitride Glasses (MPO_{3-3y/2}N_y);[M=Li,Na,K,etc...]

Using CHNS analysis, Munoz *et al.*^{42, 52} and others have validated the ammonolysis reaction, Eq. 2, and the N/P ratios calculated through careful weight loss measurements before and after ammonolysis. The reaction, shown in Eq. 2, shows the compositional integration of nitrogen in the metaphosphate glasses.

$$MPO_3 + yNH_3 \rightarrow MPO_{3-3y/2}N_y + \frac{3}{2}(y)H_2O$$
 Eq. 2

De Souza *et al.*^{42, 46, 53} have determined the concentration of nitrogen in oxy-nitride glasses from the WCF, Eq. 3, which occurs during the ammonolysis reaction. In their studies, the WCF, the formula weight (FW) of the base glass, and the weight exchange (W_E), Eq. 4, were used to accurately predict the corresponding N/P ratios and MFNs, Eqs. 5-6, for LiPON and NaPON glasses.

Weight Change Fraction =
$$WCF \equiv \frac{m_f - m_i}{m_i} \equiv \frac{mass(MPO_{3-3y/2}N_y) - mass(MPO_3)}{mass(MPO_3)}$$
 Eq. 3

$$W_E = \frac{3}{2}AW(X) - AW(N); [X = O \text{ or } S]$$
 Eq. 4

$$N/P = y = \frac{FW(MPO_3)(-WCF)}{\left(\frac{3}{2}AW(O) - AW(N)\right)} = FW(MPO_3)\frac{(-WCF)}{W_E}$$
 Eq. 5

Mass Fraction Nitrogen =
$$MFN = \frac{yAW(N)}{FW(MPO_3) - \frac{3}{2}yAW(O) + yAW(N)}$$
 Eq. 6

The W_E is defined by the weight change that occurs during the nitridation reaction in which 3/2 anions (oxygen or sulfur) are replaced by 1 nitrogen atom. From this definition, W_E is 9.992 g/mole N for an oxygen to nitrogen exchange, and 34.091 g/mole N for a sulfur to nitrogen exchange.

NaPSON MOSN Glasses (Na₄P₂S_{7-x-3/2 ν z}O_{x-3/2 ν (1-z)N ν)}

Given the more complex chemistry of this system, the ammonolysis reaction of the $Na_4P_2S_{(7-x)-3/2yz}O_{x-3/2y(1-z)}N_y$ glasses can be described through the chemical reaction given in Eq. 7, which can be expressed as a function of the base glass chemistry (x), concentration of nitrogen (y), and exchange parameter (z). From this reaction, the final composition of the nitrided NaPSON glasses were determined by selecting values of (x, y, z) for the MOSN glasses that simultaneously agree with the experimentally measured WCF and MFN values. Through modification of Eqs. 2-6, this approach can be applied to determine the N/P ratio and is given in Eq. 7.

$$Na_4P_2S_{7-x}O_x + yNH_3 \rightarrow Na_4P_2S_{7-x-3/2}O_{x-3/2}$$

In the case of MOS glasses, NH₃ has the potential to react with both oxygen and sulfur anions to yield a range of possible compositions determined by z. To compare the proposed reaction products to the experimental results, an expression for WCF_{Model} and MFN_{Model} will be presented which describe the nitrogen containing glass chemistry.

Knowing the base glass chemistry, x, values for y and z can be determined by fitting the WCF_{Model}, Eq. 8, to the experimental WCF given in Eq. 3.

$$WCF_{Model} = \frac{FW_{MOSN} - FW_{MOS}}{FW_{MOS}}$$
 Eq. 8

As the basis for the theoretical weight change, the composition dependent formula weight of the base glass, $FW_{MOS}(x)$, was calculated for the compositional series, $Na_4P_2S_{7-x}O_x$, using Eqs. 9a-b, below. In these expressions, AW(i) represents the atomic weights of each corresponding element i. The theoretical formula weight of the MOSN series, $Na_4P_2S_{7-x-3/2yz}O_{x-3/2y(1-z)}N_y$, is expressed numerically as a function of (x, y, z) in Eq. 10.

$$FW_{MOS}(x) = 4AW(Na) + 2AW(P) + (7-x)AW(S) + xAW(O)$$
 Eq. 9a

$$FW_{MOS}(x) = 154 + (7 - x)32.06 + x16.00$$
 (g/mole) Eq.9b

$$FW_{MOSN}(x, y, z) = FW_{MOS}(x) + yAW(N) - zy\frac{3}{2}AW(S) - (1-z)y\frac{3}{2}AW(O)$$
 Eq.10

Based on the ammonolysis reaction in Eq. 7, an expression for the theoretical WCF of the corresponding MOSN formula (x, y, z) can be determined by combining Eq. 8-10, and is derived in Eq. 11a-b.

$$WCF_{\text{Model}} = \frac{\left[FW_{MOS}(x) + yAW(N) - \frac{3}{2}yzAW(S) - \frac{3}{2}y(1-z)AW(O) \right] - FW_{MOS}(x)}{FW_{MOS}(x)}$$
 Eq. 11a

$$= \frac{yAW(N) - \frac{3}{2}yzAW(S) - \frac{3}{2}y(1-z)AW(O)}{FW_{MOS}(x)}$$
 Eq. 11b

The experimental MFN values, MFN_{expt.}, in the MOSN glasses were determined from the CHNS analysis. To validate the proposed values of (x, y, z) for the MOSN glass formula, the MFN_{Model} was calculated using Eq. 12, and compared to the experimentally measured value.

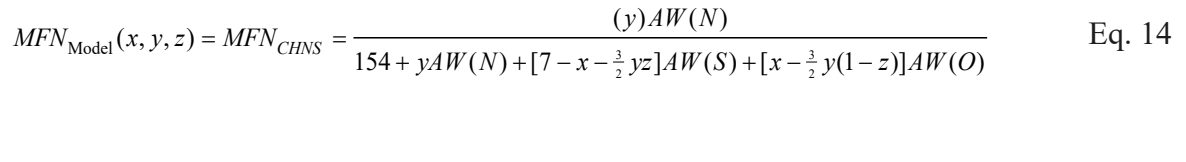
$$MFN_{\text{Model}}(x, y, z) = \frac{yAW(N)}{4AW(Na) + 2AW(P) + yAW(N) + \left(7 - x - \frac{3}{2}yz\right)AW(S) + \left(x - \frac{3}{2}y(1 - z)\right)AW(O)} \quad \text{Eq. 12}$$

Determining the N/P ratio solely based on the knowledge of x and the ammonolysis reaction poses difficulty considering the large number of possible solutions for (y, z).

Modeling the N/P via Simultaneous Fit of WCF_(exp.) and MFN_(CHNS)

The N/P ratio was therefore determined by simultaneously fitting both the WCF_{Model} and MFN_{Model} from (x, y, z) values to the experimentally measured WCF, and MFN values. This model allows for the determination of both (y, z) values directly from the experimental results without any assumptions. First, the values of the predicted MOSN compositions were determined by following Eq. 13 over a range of y-values which agreed with the experimental WCF measurements. Next, the range of possible N/P ratios, for a given y-value, were resolved by establishing a z-value corresponding to a MFN_{Model} value that satisfied the conditions described in Eq. 14.

$$WCF_{Model}(x, y, z) = WCF_{Exp.} = \frac{(y)AW(N) - \frac{3}{2}yzAW(S) - \frac{3}{2}y(1-z)AW(O)}{FW_{MOS}(x)}$$
 Eq. 13



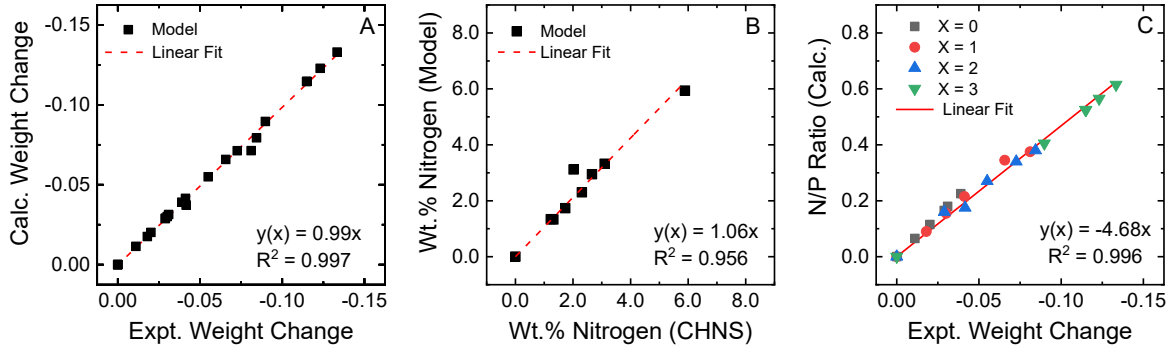


Figure 8a-c. a) Correlation between WCF_{model} vs. WCR_{exp} for simultaneous fit solution b) Correlation between MFN_{model} vs. MFN_{exp} for simultaneous fit solution. c) Calculated N/P ratio for the different base glasses.

The MOSN formulas (x, y, z) were found to agree with both with the experimentally measured WCF and MFN values, Fig. 8a-c. As seen in Fig. 8a, the calculated WCF_{Model} values were found to be in very good agreement with the WCF_{Expt.} values. Fig. 8b. shows a linear relationship with the expected slope of 1 (1.06) and intercept of 0. From this information, the (y, z) values were extracted for each sample to calculate the N/P ratio and are plotted versus the experimental WCF in Fig. 8c and as a function of ammonolysis time in Fig. 9.

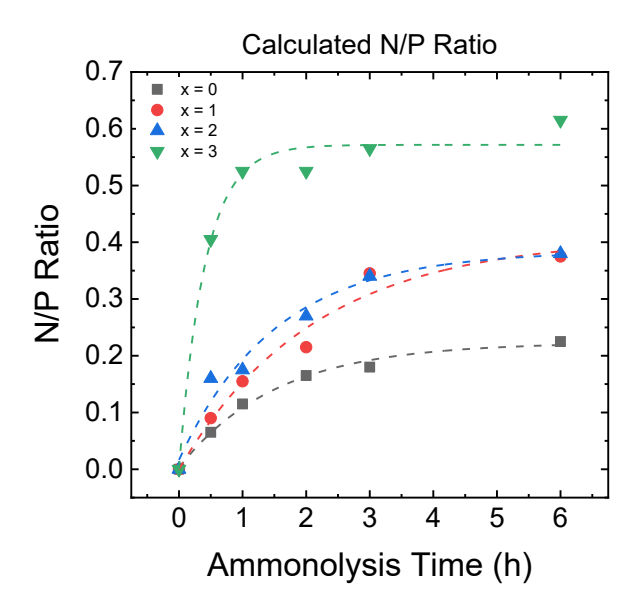


Figure 9: Processing time dependent N/P ratio for NaPSON glasses, calculated using the generated model.

N/P Limits in Alkali Phosphate Glasses

The nitrogen solubility in phosphate glasses is dictated by at least two things: the viscosity of the liquid and the melt chemistry. The viscosity is believed to limit the diffusion rate of NH₃ into the melt, while the covalent bonding dictates the maximum concentration of nitrogen that can be incorporated into the glass. It is important to note that the need for a liquid is only a requirement for glass formation - not the incorporation of nitrogen. Silicon nitride (Si₃N₄), silicon aluminum oxy-nitride (SiAlON), and boron nitride (BN) have all been found to incorporate nitrogen in the solid-state ⁵⁴⁻⁵⁶. It has also been shown that phosphorus nitride (P₃N₅) can be synthesized in the solid-state through the ammonolysis reaction of phosphorus pentasulfide given in Eq. 15. ^{36, 39}

$$6P_2S_5 + 20NH_3 \xrightarrow{\Delta} 4P_3N_5 + 30H_2S$$
 Eq. 15

Schnick et al. has reported P₃N₅ to be the highest concentration of nitrogen achievable, reaching the theoretical max N/P = 1.67 for a phosphorus compound under standard temperature and pressure. Through ammonolysis, ammonia was determined to not interact with the ionic, nonbridging sites, but instead with the covalent, bridging sites, and terminal (P=X) sites present within the glass during the ammonolysis process. With the addition of alkali ions and the formation of non-bridging (ionic) sites the theoretical maximum nitrogen concentration decreases from N/P = 1.67 in the unmodified P_3N_5 (R = 0.0) chemistry, to N/P = 1.33 in the metaphosphate (R = 1.0), reaching an N/P = 1.0 in the pyrophosphate (R = 2) compositions. The upper limit of nitrogen incorporation was investigated for metaphosphate compositions, MPO₃, M = Li or Na, based oxynitride glasses and was found to achieve a maximum experimental N/P = ~ 0.67 or MPO₂N_{0.67} through direct ammonolysis 41, 46, 57 compared to the theoretical limit of 1.33. The discrepancy in the theoretical limit observed at higher modifier concentrations can be attributed to the diffusion limiting kinetics caused by the increase in viscosity. Day et al. 37, 58 incorporated a small concentration of halide salts to LiPO₃ to plasticize the network, reducing the viscosity, and increased the maximum N/P to ~0.7. However, Day et al. 53, 58 still did not achieve an N/P ratio close to the theoretical max N/P = 1.33 for the metaphosphate chemistry. Conclusively, the viscosity of the glass melt plays a large role in the ammonolysis process.

However, the way in which nitrogen enters the glass structure must also be considered in determining the limit of the N/P ratio at a given modifier concentration. Many have reported for metaphosphate glasses that nitrogen is incorporated into the structure in two ways: trigonally coordinated nitrogen (N_t), and linearly coordinated nitrogen (N_d)^{34, 37, 46}. These two nitrogen species are not structurally equivalent. As shown in Eq. 16, the formation of N_t species consumes

3/2BOs to produce a glass with a higher network density. The N_d species are seen to be more advantageous to glass formability as they consume $\frac{1}{2}$ BO and a NBO by converting the non-networking P=X sites to networking P=N-P sites as shown in Eq. 17. The formation of both species is critical to achieving the maximum N/P ratio at a given R-value.

$$3NaPO_3 + N_T \rightarrow 3(NaPO_{2.5}N_{T(0.\overline{33})}) - \frac{3}{2}(BO)$$
 Eq. 16

$$2NaPO_3 + N_D \rightarrow 2(NaPO_{2.25}N_{D(0.5)}) - NBO - \frac{1}{2}BO$$
 Eq. 17

Reports by De Souza *et al.* ^{46, 52, 59} have shown with Raman spectroscopy that the N_t species is the dominant form of nitrogen in both LiPON and NaPON glasses with N/P < 0.33. Significant concentrations of the N_d species are only reported in glasses containing N/P > 0.33, where the preferential formation of N_d over N_t species is observed⁴³. This behavior becomes increasingly important at higher modifier concentrations. Additionally, the max N/P ratio is controlled by the fraction of each nitrogen species incorporated into the invert glasses.

Processing Effects on N/P ratio

Reaction Kinetics

It is important to state that the ammonolysis temperature dictates the melt viscosity of the base glasses and that the incorporation of nitrogen increases the T_g . It has been shown that the melting temperature relative to the T_g determines the viscosity of the liquid⁶⁰. Therefore, as nitrogen enters the MOS liquid the viscosity of the melt will begin to increase continuously until the end of the experiment, where chemical equilibrium is achieved or thermal decomposition

occurs. Thus, when the processing temperature and sample size are held constant, the system becomes self-limiting as nitrogen can no longer diffuse into the melt.

The liquid behavior of the different MOS base glasses are controlled by the eutectic reported in the Na₄P₂S_{7-x}O_x system with the liquidus temperature reaching as low as 450°C in the Na₄P₂S_{4.5}O_{2.5} composition⁶¹. Thus, given a fixed processing temperature for all samples, the glass with the lowest viscosity would enable the most rapid diffusion of nitrogen into the liquid structure. The reaction kinetics appear the fastest in the highest oxygen containing glasses and become sluggish in the absence of oxide bonds in the glass. The kinetics, however, do not explain the difference in weight loss observed for each sample series. The solubility of nitrogen is then less associated with the kinetics and more with the SRO structures present within the glass as previously stated.

Thermal Properties

Glass Transition Temperature (Tg) Considered Using N/P Model

The measured T_g 's were plotted in Fig. 10 versus a series of N/P ratios determined with the presented model, showing a systematic increase as a function of nitrogen concentration. The composition dependent T_g measured for the MOSN glasses exhibits a peculiar trend which is tied to the base glass chemistry. It is observed in the Na₄P₂S_{7-x}O_x series that the T_g remains almost constant at ~190°C for 0 < x < 3 as a result of the disproportionation reaction that occurs with the addition of oxygen⁶¹. Upon nitridation, however, the concentration of oxygen in the base glass has a much different effect on the thermal properties. Similar to the trend in the measured WCF, the relative increase in T_g for the higher oxygen containing, Na₄P₂S₄O₃, glass was much greater than

that of the Na₄P₂S₇, sulfide composition as shown in Fig. 4. Similar to the increase seen in NaPON, the larger change in thermal properties can be correlated to an increase in the cross-link density of the glass structure, Fig. S5. The concentration of BOs and their local environment have been found to play a critical role in the formation of the nitrogen containing glass network, as will be discussed in the following sections.

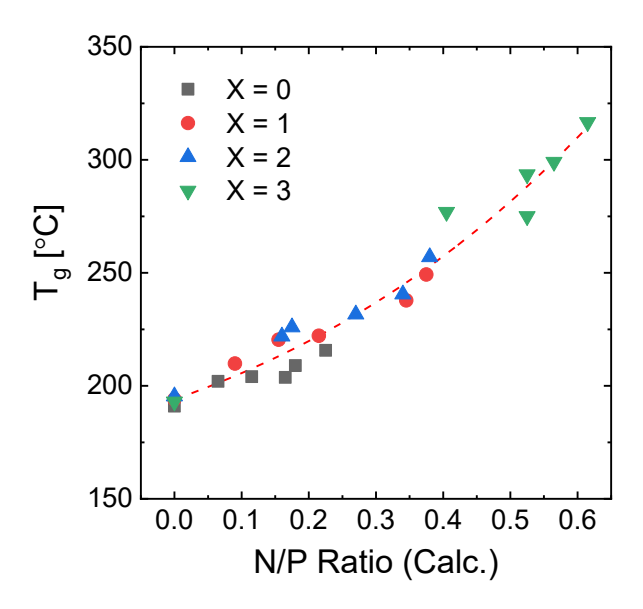


Figure 10: The T_g dependence on the N/P ratio calculated using the model for NaPSON glasses with an R = 2 where the different symbols denote the composition of the base glasses. Nitrogen concentrations were found to increase with oxygen concentration in the base glass. The line has been added as a guide to the eye.

Structural Model of Direct Nitride NaPSO Glasses

Review of NaPSO SRO Structure

To better understand how nitrogen is incorporated into the $Na_4P_2S_{7-x}O_x$ glass series, the reaction Eq. 7 will be approached from the standpoint of the SRO structures that make up the

covalent glass network (P-X-P) and terminal sites (P=X), where X = O or S. As reported by Kmiec *et al.*³⁰, the distribution of SRO species changes dramatically with the incorporation of oxygen in the Na₄P₂S₇ glass via a disproportionation reaction. This is exemplified in Fig. S6 that shows how the structure is dominated by the P¹ anion in the Na₄P₂S₇ glass but is quickly replaced by PS_{4-x}O_x (P⁰) and PO₃ (P²) anions with increasing amounts of oxygen. The greatest distribution of SRO species is observed in the Na₄P₂S₄O₃ glass structure, with almost equal populations of P¹ (20%), P⁰ (20%), and P² (30%) species.

SRO Structural Evolution of Na₄P₂S_{7-x}O_x Glasses via Ammonolysis Process

The ionic SRO structures were not considered in the reaction pathways of the ammonolysis process. Thus, the P⁰ species (PS₄ and PSO₃) were assumed unaffected by the ammonolysis process and, when present in the melt, would prevent nitrogen uptake to that SRO species. Fig. S6, shows the most abundant networking SRO species in the base glasses are the P^{1(S)} and P² anions. From these structures, different reactions were generated to describe the SRO structures formed at different concentrations and configurations of nitrogen.

Due to the observed preferential reactivity, the ammonolysis reaction is considered a path dependent process in the Na₄P₂S_{7-x}O_x system. The disproportionation reaction that occurs in the Na₄P₂S_{7-x}O_x system with the incorporation of oxygen results in a much higher concentration of non-networking PS_{4-x}O_x P⁰ species, and polymeric P² species in the Na₄P₂S₅O₂ and Na₄P₂S₄O₃ compositions. This is further emphasized by the MIR spectral comparison given in Fig. 11, showing strong changes in the oxide modes.

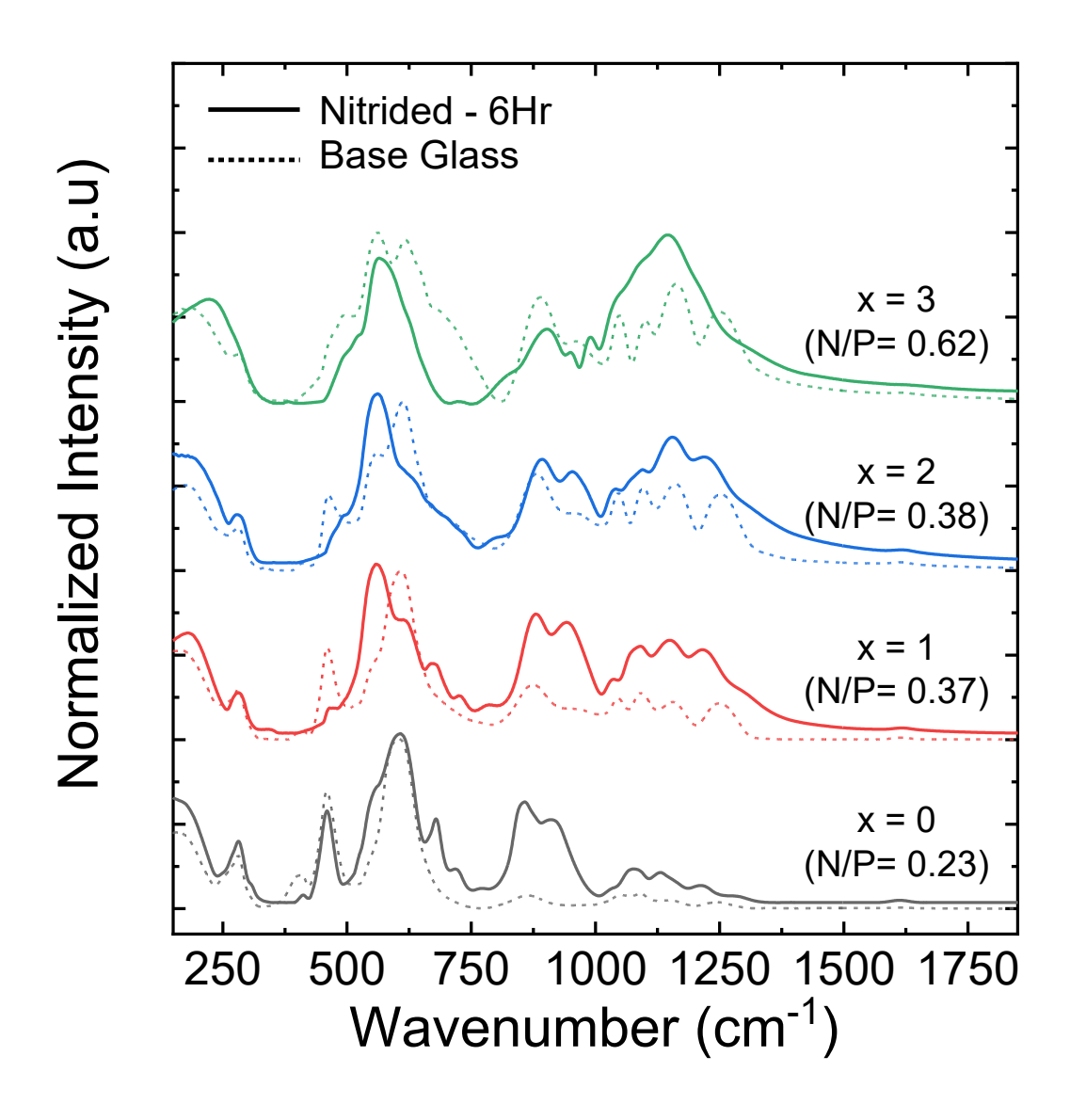


Figure 11. MIR spectra of Na₄P₂S_{7-x}O_x glasses directly nitrided for 6 h. to allow for comparison of the different reaction pathways.

Ammonolysis of Na₄P₂S₇

The pure sulfide, Na₄P₂S₇, base glass structure is predominantly comprised of P^1 anions (85%), with the remainder consisting of P^{1P} and $P^{0(S)}$ anions as impurity phases, which is supported by the MIR and Raman spectra, Figs. 6 and 5a, respectively. However, upon ammonolysis, both

spectra suggests the SRO structure is slowly shifting from a predominance of P¹ species to P⁰.

As described, nitrogen appears only to react with covalent P-S-P and P=S bonds to form PSN tetrahedral units. Evidence of PSN species is clearly observed in the MIR spectra, Fig. 6. Typically, these modes would be associated with P-O-P bonds in purely MOS glasses, but in these MOSN glasses, there exists very few accompanying oxide modes to support this claim. Instead, these modes are assigned to the v(P-N_t) modes based on their striking agreement with features in the P₃N₅ spectra^{35,50}. From these observations it is reasonable to assume nitrogen enters the system primarily in the form of N_t species through P¹ anions. The assumption is bolstered by the evidence of PS₄ SRO species being formed in the MIR spectra.

Ammonolysis of Na₄P₂S₆O

As the result of the disproportionation reaction in the Na₄P₂S_{7-x}O_x glass system, the SRO species distribution of the Na₄P₂S₆O base glass is comprised of (~60%) P¹ anions, (~15%) P² anions, and (~15%) PS_{4-x}O_x (P⁰) anions. The remainder of the Na₄P₂S₆O glass structure is comprised of P^{1P} defect units. This is seen in the MIR spectra, Figs.11 and S3. Upon ammonolysis, the mode assigned to the ν P-S-P in the P¹ anion is steadily consumed through the reaction and replaced by a series of modes at higher frequencies. Similarly to the pure sulfide glasses, the two δ (P-N) modes centered at 680 cm⁻¹ and 720 cm⁻¹ also appear in this series and are in good agreement with the P₃N₅ spectra^{38, 39}. Considering the covalent P-S-P bonds are consumed in the nitridation process, it is reasonable to assume the changes observed here are associated with the formation of the ν (P-N_t) mode. Senevirathne *et al.*⁵⁰, investigated the P-N_d bond present in the Li₂PO₂N crystalline phase and found π -bonding present in the N_d species produces vibrational

modes at higher frequencies, ranging from 850 cm^{-1} to 1250 cm^{-1} . It important to note that the modes between 680 cm^{-1} and 720 cm^{-1} are only present in the sulfur-rich samples, which are tentatively assigned $v(P-N_t)$ modes in $PS_{4-x}N_x$ tetrahedra.

Ammonolysis of Na₄P₂S₅O₂

The SRO species distribution of the Na₄P₂S₅O₂ base glass is comprised of (~45%) P¹(S) anions, (~5%) P¹(O), (~20%) P² anions, and (~20%) PS_{4-x}O_x P⁰anions. The remainder of the Na₄P₂S₅O₂ glass structure is comprised of P^{1P} defect units. With further additions of oxygen and the progression of the disproportionation reaction in the base glass, P¹ anions are converted to P⁰ anions to become the dominant sulfide species in the structure, as shown in the Raman spectra in Fig. 5b. The increasing concentration of ionic species limits the covalent sulfide (P-S-P) bonds from reacting with the NH₃ and producing PS_{4-x}N_x tetrahedra. Instead, the covalent oxide (P-O-P) bonds were found to readily form PO_{4-x}N_x tetrahedra upon ammonolysis subsequently leading to the formation of an oxy-nitride host network for PS₄ and PSO₃ non-networking species.

Through the ammonolysis of the $Na_4P_2S_5O_2$ base glass, the $v_{as}(P\text{-O-P})$ modes initially increased then began to decrease relative to the surrounding modes. Upon decreasing, these modes became more resolved and narrowed. This line shape change is indicative of the conversion of P-O-P bonds to P-N-P bonds, and shown in Fig. 11. Additionally, the bands associated with the v_{as} (O-P-O) / NBO of P^2 species broaden in intensity relative to the surrounding NBO peaks with longer processing times. This is due to the superposition of P-O and P-N modes through the formation of P=N-P bonds, which form and amplify the existing modes in the region.

Ammonolysis of Na₄P₂S₄O₃

Finally, the Na₄P₂S₄O₃ composition was found to possess the most uniform distribution of SRO species of the base glasses studied. The SRO species distribution of the Na₄P₂S₄O₃ glass is comprised of (~20%) $P^{1(S)}$ anions, (~10%) $P^{1(O)}$, (~33%) $P^{2(O)}$ anions, and (~33%) $PS_{4-x}O_x$ P^0 anions; the remainder comprised of (~3%) P^{1P} defect units. The most dramatic change in the Raman and MIR spectra is observed after just 0.5 h, Fig. 5d and 7, with the disappearance of the modes associated with P^{1(S)} species and a decrease in modes corresponding to P^{2(O)} species. The highest oxygen containing chemistry has been found to readily form a prominent host network of $PO_{4-x}N_x$ tetrahedra due to the high reactivity of NH₃ in covalent oxide species. Because the base glass has a high concentration of P^{2(O)} anions, nitrogen was found to predominantly enter the structure through this reaction pathway. As a portion of the P^{2(O)} units are consumed, the broad v_{as}(P-O-P) mode of P^{1(O)} species, centered at 950 cm⁻¹, begins to split into two modes with increased ammonolysis times. These two new modes are in good agreement with literature values reported for $v(P-N_t)$ modes in crystalline P_3N_5 . Thus, they are assigned to the v(P-N) in oxygen $P^{1(N)}$ SRO species, $[PO_3N_{0.33}]^{2-}$, with an N_t bond⁵⁰. With the initial addition of nitrogen, the modes associated with the NBOs of the P⁰, P¹, and P² species in this region broaden as a result of overlap with formation of new $v(P-N_d)$ modes. By interpreting the line shape of this envelope as a function of nitrogen content, preferential growth of the v_{as}(O-P-O) mode at 1145 cm⁻¹ is observed and can be assigned to the NBO $[PO_{3-3x/2}N_x]^-$ anion. The shift of this mode to lower wavenumber suggests nitrogen weakens the field strength of the ionic NBO species.

Nitrogen Incorporation Mechanisms via P2X7 Anions

It has been proposed by Day *et al.*^{37,53} that ammonia reacts with phosphate glass melts to incorporate nitrogen in to the structure following Eq. 2 to form either N_t or N_d species. This, however, is not completed in a single elementary reaction, but instead requires a set of intermediate steps to form the proposed nitride species. De Souza *et al.*⁴⁶ have reported a much greater concentration of N_t species in the LiPON and NaPON glasses over a wide range of N/P ratios. The disproportionate concentration of nitrogen species in the metaphosphate glass structure, as observed via Raman spectroscopy, suggests a more favorable reaction pathway(s) for the formation of N_t species. Here, a set of reaction mechanisms that describe the intermediate steps of the ammonolysis process necessary to form both N_t and N_d in phosphate glasses is proposed. In this section, the reaction mechanisms for nitrogen incorporation in pyro-phosphate P^{1(O)} and pyrothiophosphate P^{1(S)} anions is discussed.

As determied from the Raman spectra, Figs. 5a-d, the ammonolysis process was found to generate non-networking P^0 species upon the incorporation of nitrogen to the sulfide and oxysulfide glasses. Given in Eq. 18-19, a set of 3 reaction mechanisms that occur when NH₃ reacts with the P_2S_7 anion in a dilute nitrogen environment.

Reaction Scheme 1. Reaction pathways for the ammonolysis of $[P_2S_7]^{4-}$ anions to form, $[(P^{1N})_3N_T]^{6-}$ (Cluster), $[PS_4]^{3-}$ (Monomeric), and $[P^{1S}-P^{2N}(P^{1N})_2N_T]^{7-}$ (Polymeric) species in Eqs. 18a-b and 19, respectively.

In the first mechanism, Eqs. 18a-b, the bridging site of the P_2X_7 anion (P-X-P; X =O or S) [A] is targeted by NH₃ to form a primary amine (P-NH₂) and a thiol/hydroxyl (P-XH) group. As a result, the following non-networking intermediate species, $PX_3NH_2^{2-}$ [B] and HPX_4^{2-} [C], are produced which are critical for the progression of the ammonolysis process. During this initial stage of the reaction, the NH₃ is retained in the intermediate products, and no H₂S is generated to contribute to the observed weight loss. In the final reaction of Eq. 18a, the primary amine group of the $[P^0-NH_2]^{2-}$ anion reacts with the bridging site of a neighboring P_2S_7 anion to form H₂S and a P_3N_t junction as the product.

The second mechanism, Eq. 18b, describes the reaction pathway for the formation of P^0 species. In this case, P^0 species are formed through a cation exchange reaction between [C] and

[A] to form the intermediate species [A*], $HP_2S_7^{3-}$ and a P^0 unit as the product. The cation exchange in this case is driven by the steric repulsion of the proton associated with the Na_2HPS_4 species. For this reason, it is hypothesized that the free energy of the products PS_4^{3-} and $H_2P_2S_7^{3-}$ are lower than the initial intermediate species.

In the third mechanism, Eq. 19, the bridging site of the P_2X_7 anion (P-X-P; X =O or S) reacts with NH₃ to form a secondary amine (P-NH-P) group and H₂S. In this stage, the two phosphorus atoms are bonded by nitrogen, but the ammonolysis reaction is not complete until the final proton is removed from the secondary amine, and the P_3N_t junction is formed. For this to occur, the P-NH-P group must react with a thiol/hydroxyl group (P-XH) produced in the second reaction mechanism, Eq. 18b, to complete the N_t reaction. Unlike the first mechanism, the N_t structures formed via this pathway create a polymeric structure with a P-S-P-N-P backbone. The first incorporation mechanism, Eq. 18a-b, was found to be the rate limiting step in the ammonolysis process, as all subsequent elementary reactions require the intermediate products formed in this reaction.

Reaction Scheme 2. Reaction pathways for the ammonolysis of $[P_2S_7]^{4-}$ anions to form, $[(P^{1N})_3N_T]^{6-}$ (Cluster), and $[P^{1N}-P^{2N}-P^{1S}]^{6-}$ (Polymeric) species in Eqs. 20a-b, and 21, respectively

In a nitrogen rich structural environment, NH₃ can react with the dimer species to form either a primary amine (P-NH₂) [B] and a thiol (P-SH) [C] group, or a secondary amine group (P-NH-P) [D] and H₂S. Under this condition, the intermediate species, formed in Eqs. 20a-b, have a much greater probability of interacting with another intermediate species as opposed to reacting with a base glass species. The formation of N_d species in P₂X₇ anions follows the mechanism given in Eq. 20a, with the initial NH₃ reaction producing intermediate thiol/hydroxyl (P-XH) and a primary amine (P-NH₂) groups. This is further exemplified in Eq. 20b, where the secondary amine [D] species is shown to react with the non-networking, HPS₄³⁻ intermediate species [C], to form a

 $(P^{1N})_3N_t$ cluster instead of a branching N_t structure. Given the low relative abundance of N_d species reported in MPO_{3-3x/2}N_x glasses, we hypothesize that N_d species are formed through the reaction of P-HN₂ and P=X bond, but only when there are no longer an available reaction pathway to form N_t sites in the localized region. A possible reaction product for this mechanism can be seen in Eq. 21 with N_d species forming short P^{1N} -N=P-X- P^{1X} chains. This method of incorporation only allows for N_d species to from in the melt once N_t species have been formed which is in agreement with reports on LiPON and NaPON glass^{37, 46, 50}.

Nitrogen Incorporation Mechanisms via PO3 SRO Species

Previous reports have shown that PO₃⁻ anions occupy several IRO structures within alkali metaphosphate glasses, which is especially important in the NaPSO glass system, with an R = 2 (Na₄P₂X₇), as we expect to see PO₃ anions occupy small rings (P₃O₉)³- and short chains (P₃O₁₀)⁵- in the base glasses^{30, 62, 63}. As reported, nitrogen has the ability to increase the connectivity of these SRO species^{59, 64}. Therefore, the IRO structure of the MON glass fragment is dictated by both the concentration of P² species and the SRO units they are connected too. Although briefly discussed in previous reports, a complete multi-step reaction mechanism for the incorporation of nitrogen in metaphosphate glasses has not been reported^{41, 65, 66}. Here, a complete reaction scheme that describes all the intermediate steps of the ammonolysis process necessary to form both N_t and N_d in meta-phosphate (PO₃⁻) anions is proposed. As shown in Eqs. 22-24, there are at least three possible reaction mechanisms for ammonia to react with PO₃⁻ anions in these highly modified MOSN glasses.

Reaction Scheme 3. Reaction pathways for the ammonolysis of $[PO_3]^-$ anions to form, $[(P^{2N})_3N_T]^{3-}$ in Eqs. 22-23.

In the first mechanism for meta-phosphate species, Eq. 22, a bridging oxygen (P-O-P) site in the PO₃⁻ anion reacts with NH₃ to form hydroxyl (P-OH) and primary amine (P-NH₂) groups. The initial reaction allows ammonia to be incorporated into the structure to form intermediate species needed, necessary for the formation of N_t species, without generating H₂O. The intermediate reaction in Eq. 22, shows the primary amine can react with other PO₃⁻ anions to form H₂O and P₃N_t junction. In the second mechanism, Eq. 23, a bridging oxygen in the PO₃⁻ anion (P-O-P) reacts with NH₃ to form a secondary amine (P-NH-P) group and H₂O. In this intermediate stage, the two phosphorus atoms are bonded by a nitrogen atom, but the reaction is not complete until P₃N_t junction is formed and the final proton is removed. For this to occur, the P-NH-P group must react with a hydroxyl group (P-OH) produced in the first mechanism, Eq. 22, to complete the N_t reaction.

As previously stated, it has been hypothesized that N_d species are formed through the reaction of P-HN₂ and P=X bond, Eq. 24, but only when there are no longer available reaction pathways to form N_t sites in the localized region.

Reaction Scheme 4. The ammonolysis reaction pathway for $[PO_3]^-$ anions to form, $[P^{2O}-(P^{2N})_2N_d]^{3-}$ species in Eq. 24.

This hypothesis can be applied to all covalent species in the current glass system and suggests that as the concentration of ionic species increases, the concentration of N_d species should also increase. Evidence for these conditions are best observed in the $Na_4P_2S_4O_3 + N$ series given the structure is comprised of predominately monomeric $PS_{4-x}O_x^{3-}$ and polymeric PO_3^{-} anions. The Raman and MIR spectra of this series, Figs. 5d and 6, reveals almost no change to the sulfide species, but the largest change is between 1000 cm^{-1} and 1400 cm^{-1} with new modes assigned to $v(P-N_d)$. Although the above reactions, Eqs. 22-24, are shown to terminate with other oxide units, it is reasonable to consider additional reaction pathways where the intermediate species react with sulfide or MOS SRO units.

Formation Mechanisms of Possible MOSN Intermediate Range Order (IRO) Structures

Following the reaction mechanisms proposed in Eqs. 22-24 and knowledge of the SRO species, it is possible to identify the IRO structures in these MOSN glasses, it is likely that there is a distribution of hydroxyl (P-OH) and thiol (P-SH) groups present in the melt during the reaction. If one of these two groups were a local minority, it would be forced to react with different SRO units. Given the sulfide-rich nature of the $Na_4P_2S_{7-x}O_x$ series tested, it is reasonable to assume a uniform distribution of oxygen species throughout the sulfide glass structure. An example of this is given in Eq. 25, where NH_3 is shown to react with a $P_2O_7^{4-}$ anion to form a hydroxyl (P-OH)

and primary amine (P-NH₂) group. In this case, the hydroxyl groups are shown to react with surrounding sulfide containing species to form MOSN IRO structures. This mixed species reaction is also capable of producing mixed anion structures connected to N_d species, as shown in Eq. 26. In this scenario, a PS₃(NH₂) tetrahedra is grafted to a P-O-P chain via reaction of a primary amine to from a polymeric MOSN structure.

Reaction Scheme 5. The ammonolysis reaction pathway of $[P_2O_7]^{4-}$ intermediates reacting with $[P_2S_7]^{4-}$ anions to form isolated MOSN clusters (Eq. 25). The reaction pathway for $[P_2S_7]^{4-}$ intermediates reacting with $[PO_3]^{-}$ anions to form polymeric MOSN networks (Eq. 26).

Conclusions

Bulk samples of Na₄P₂S_{7-x}O_x glasses were melted for incremental amounts of time in an NH₃ atmosphere to incorporate nitrogen into the glass structure. The N/P ratios calculated from weight loss measurements show excellent agreement with CHNS results. Raman and MIR spectroscopy were used to identify the reaction mechanisms for nitrogen incorporation into

 $Na_4P_2S_{7-x}O_x$ glasses. The N_t species were determined to form preferentially when reacted with P_2S_7 anions though a reaction mechanism producing P^0 species in the process. Nitrogen incorporation into PO_3 anions is a direct process, requiring SRO units to only have be in close proximity and were found to dictate the maximum solubility of nitrogen in the glass. Therefore, in the future, it would be advantageous to be able to engineer the type of nitrogen incorporated into the glass to further increase the tune-ability of the materials properties.

Acknowledgements

Funding for this work was provided by the ARPA-E of the Department of Energy through contract number DE-AR0000654 and DE-AR-0000778. Additional funding for this work was provided by the Vehicle Technology office within the Department of Energy though the contract DE-EE0008852 and the National Science Foundation under grant number DMR 1936913. We wish to thank ISU Chemical Instrumentation Facility staff member Dr. Sara Cady for assistance pertaining to the PE 2100 CHN/S elemental analysis results included in this publication. Purchase of the Perkin Elmer 2100 Series II CHN/S analyzer used to obtain results included in this publication was supported in part by the National Science Foundation under Grant No. DBI 9413969. Additional thanks to Madison Olson, Adriana Joyce, and Jacob Lovi for help in the collection of the experimental data.

ASSOCIATED CONTENT

Supporting Information (SI)

Tabulated compositional and thermal data of MOSN glasses; Diagram of ammonolysis furnace system; MIR spectral series of the Na₄P₂S₆O and Na₄P₂S₅O₂ compositions at variable ammonolysis times; The Tg comparison of NaPSON to NaPON glasses as a function of the N/P ratio; The glasses SRO unit population of Na₄P₂S_{7-x}O_x base glass compositions;

List of Figures

- Figure 1. Measured weight loss from the ammonolysis of 5g bars of various Na₄P₂S_{7-x}O_x glasses as a function of processing time. Larger weight losses are observed in samples that contained greater concentrations of oxygen. Lines act as a guide to the eye.
- Figure 2. Compositional analysis of nitrogen for the Na₄P₂S₅O₂ + N series determined via CHNS measurements reported in weight percent. Dotted lines are guides to the eye only, based on inferences from the WCF shown in Fig. 1.
- Figure 3. Example DSC Thermograms of the Na₄P₂S₅O₂+N glass series measured with a heating rate of 20°C/min, highlighting the effect ammonolysis time has on the glass transition temperature (T_g).
- Figure 4: Measured T_g's from the ammonolysis of 3-5 g bars of various Na₄P₂S_{7-x}O_x glasses as a function of ammonolysis time. Samples that contained greater concentrations of oxygen exhibited larger changes in the T_g.
- Figure 5. Raman spectral evolution of a) Na₄P₂S₇ +N, b) Na₄P₂S₆O+N, c) Na₄P₂S₅O₂+N, d) Na₄P₂S₄O₃+N, glasses directly nitrided for 0-6 h.
- Figure 6. MIR spectra of Na₄P₂S₇ glass directly nitrided for 0-6 h.
- Figure 7. MIR spectra of Na₄P₂S₄O₃ glass directly nitrided for 0-6 h.
- Figure 8a-c. a) Correlation between WCF $_{model}$ vs. WCR $_{exp}$ for simultaneous fit solution b) Correlation between MFN $_{model}$ vs. MFN $_{exp}$ for simultaneous fit solution. c) Calculated N/P ratio for the different base glasses.
- Figure 9. Processing time dependent N/P ratio for NaPSON glasses, calculated using the generated model.
- Figure 10. The T_g dependence on the N/P ratio calculated using the model for NaPSON glasses with an R=2 where the different symbols denote the composition of the base glasses. Nitrogen concentrations were found to increase with oxygen concentration in the base glass. The line has been added as a guide to the eye.
- Figure 11. MIR spectra of Na₄P₂S_{7-x}O_x glasses directly nitrided for 6 h. to allow for comparison of the different reaction pathways.

References

- 1. Zhao, Y.; Adair, K. R.; Sun, X. Recent developments and insights into the understanding of Na metal anodes for Na-metal batteries. *Energy & Environmental Science* **2018**, 11 (10), 2673-2695 DOI: 10.1039/C8EE01373J.
- 2. Hayashi, A.; Tatsumisago, M. Development of ion conducting glasses for all-solid-state batteries. *Kagaku Kogyo* **2012**, 63 (10), 770-774.
- 3. Richards, W. D.; Miara, L. J.; Wang, Y.; Kim, J. C.; Ceder, G. Interface Stability in Solid-State Batteries. *Chemistry of Materials* **2016**, 28 (1), 266-273 DOI: 10.1021/acs.chemmater.5b04082.
- 4. Ren, Y.; Chen, K.; Chen, R.; Liu, T.; Zhang, Y.; Nan, C.-W. Oxide Electrolytes for Lithium Batteries. *J. Am. Ceram. Soc.* **2015**, 98 (12), 3603-3623 DOI: 10.1111/jace.13844.
- 5. Slater, M. D.; Kim, D.; Lee, E.; Doeff, M.; Johnson, C. S. Sodium-Ion Batteries. *Advanced Functional Materials* **2013**, 23 (8), 947-958 DOI: 10.1002/adfm.201200691.
- 6. Shan, Z.; Li, C.; Yang, L.; Tian, J.; Zhou, Y.; Zhang, T. Method for manufacturing sulfur cathode of lithium sulfur battery. 2011-10189895 102280614, 20110707.. 2011.
- 7. Yang, X.; Ma, Z.; He, Y.; Bai, D. Method for manufacturing anode material for lithium ion battery. 2009-10054595 101604750, 20090709., 2009.
- 8. Li, N.; Guiver, M. D. Ion Transport by Nanochannels in Ion-Containing Aromatic Copolymers. *Macromolecules (Washington, DC, United States)* **2014,** 47 (7), 2175-2198 DOI: 10.1021/ma402254h.
- 9. Zhu, Y.; He, X.; Mo, Y. Strategies Based on Nitride Materials Chemistry to Stabilize Li Metal Anode. *Advanced science (Weinheim, Baden-Wurttemberg, Germany)* **2017,** 4 (8), 1600517-1600517 DOI: 10.1002/advs.201600517.
- 10. Porz, L.; Swamy, T.; Sheldon, B. W.; Rettenwander, D.; Frömling, T.; Thaman, H. L.; Berendts, S.; Uecker, R.; Carter, W. C.; Chiang, Y.-M. Mechanism of Lithium Metal Penetration through Inorganic Solid Electrolytes. *Advanced Energy Materials* **2017**, 7 (20), 1701003 DOI: 10.1002/aenm.201701003.
- 11. Guin, M.; Tietz, F. Survey of the transport properties of sodium superionic conductor materials for use in sodium batteries. *Journal of Power Sources* **2015**, 273, 1056-1064 DOI: 10.1016/j.jpowsour.2014.09.137.
- 12. Zhang, P.; Wang, H.; Si, Q.; Matsui, M.; Takeda, Y.; Yamamoto, O.; Imanishi, N. High lithium ion conductivity solid electrolyte of chromium and aluminum co-doped NASICON-type LiTi2(PO4)3. *Solid State Ionics* **2015**, 272, 101-106 DOI: 10.1016/j.ssi.2015.01.004.
- 13. Han, F.; Westover, A. S.; Yue, J.; Fan, X.; Wang, F.; Chi, M.; Leonard, D. N.; Dudney, N. J.; Wang, H.; Wang, C. High electronic conductivity as the origin of lithium dendrite formation within solid electrolytes. *Nature Energy* **2019**, 4 (3), 187-196 DOI: 10.1038/s41560-018-0312-z.
- 14. Buschmann, H.; Doelle, J.; Berendts, S.; Kuhn, A.; Bottke, P.; Wilkening, M.; Heitjans, P.; Senyshyn, A.; Ehrenberg, H.; Lotnyk, A.; Duppel, V.; Kienle, L.; Janek, J. Structure and

- dynamics of the fast lithium ion conductor "Li7La3Zr2O12". *Physical Chemistry Chemical Physics* **2011**, 13 (43), 19378-19392 DOI: 10.1039/c1cp22108f.
- 15. Feng, X.; Chien, P.-H.; Zhu, Z.; Chu, I.-H.; Wang, P.; Immediato-Scuotto, M.; Arabzadeh, H.; Ong, S. P.; Hu, Y.-Y. Studies of Functional Defects for Fast Na-Ion Conduction in Na3–yPS4–xClx with a Combined Experimental and Computational Approach. *Advanced Functional Materials* **2019**, 29 (9), 1807951 DOI: 10.1002/adfm.201807951.
- 16. Hayashi, A.; Noi, K.; Sakuda, A.; Tatsumisago, M. Superionic glass-ceramic electrolytes for room-temperature rechargeable sodium batteries. *Nature Communications* **2012**, 3 (May), 1843/1-1843/5 DOI: 10.1038/ncomms1843.
- 17. Wang, H.; Chen, Y.; Hood, Z. D.; Sahu, G.; Pandian, A. S.; Keum, J. K.; An, K.; Liang, C. An Air-Stable Na3SbS4 Superionic Conductor Prepared by a Rapid and Economic Synthetic Procedure. *Angewandte Chemie International Edition* **2016**, 55 (30), 8551-8555 DOI: https://doi.org/10.1002/anie.201601546.
- 18. Dietrich, C.; Weber, D. A.; Sedlmaier, S. J.; Indris, S.; Culver, S. P.; Walter, D.; Janek, J.; Zeier, W. G. Lithium ion conductivity in Li2S–P2S5 glasses building units and local structure evolution during the crystallization of superionic conductors Li3PS4, Li7P3S11 and Li4P2S7. *Journal of Materials Chemistry A* **2017**, 5 (34), 18111-18119 DOI: 10.1039/C7TA06067J.
- 19. Seino, Y.; Ota, T.; Takada, K.; Hayashi, A.; Tatsumisago, M. A sulphide lithium super ion conductor is superior to liquid ion conductors for use in rechargeable batteries. *Energy & Environmental Science* **2014**, 7 (2), 627-631 DOI: 10.1039/c3ee41655k.
- 20. Seo, I.; Kim, Y.; Martin, S. W. Characterization of thin-film electrolytes for all solid-state batteries. *J. Alloys Compd.* **2016**, 661, 245-250 DOI: 10.1016/j.jallcom.2015.11.012.
- 21. Martin, S. W. In *Handbook of Solid State Batteries, 2nd Edition*; Dudney, N., West, W., Nanda, J., Ed.; World Scientific: New Jersey, 2015; Chapter 14, pp 433-501.
- 22. Ohtomo, T.; Hayashi, A.; Tatsumisago, M.; Kawamoto, K. Glass electrolytes with high ion conductivity and high chemical stability in the system LiI-Li2O-Li2S-P2S5.
- Electrochemistry (Tokyo, Japan) 2013, 81 (6), 428-431 DOI: 10.5796/electrochemistry.81.428.
- 23. Ohtomo, T.; Kawamoto, K.; Hama, S.; Kato, Y. Sulfide glass solid electrolyte material, manufacture thereof, lithium solid state battery. 2011-173092 2013037896, 20110808., 2013.
- 24. Zhao, S. l.; Wen, J. b.; Fan, L. m.; Qin, Q. z. Development of preparation and application of LiPON thin film. *Dianchi* **2005**, 35 (6), 459-461.
- 25. Zhao, S.; Wen, J.; Yang, D.; Fu, Z. Properties and fabrication of lithium phosphorus oxynitride electrolyte thin films. *Gongneng Cailiao* **2005**, 36 (7), 1050-1052, 1055.
- 26. Dudney, N. J.; Kim, Y.; Tenhaeff, W.; Herbert, E.; Veith, G. Lithium phosphorus oxynitride solid electrolyte: Applications beyond thin film batteries. *Abstracts of Papers, 240th ACS National Meeting, Boston, MA, United States, August 22-26, 2010* **2010**, INOR-400.
- 27. Baggetto, L.; Unocic, R. R.; Dudney, N. J.; Veith, G. M. Fabrication and characterization of Li-Mn-Ni-O sputtered thin film high voltage cathodes for Li-ion batteries. *Journal of Power Sources* **2012**, 211, 108-118 DOI: 10.1016/j.jpowsour.2012.03.076.
- 28. Dudney, N. J. Thin film micro-batteries. *Electrochem.Soc.Interface* **2008**, 17 (3), 44-48.
- 29. Dudney, N. J. Glass and ceramic electrolytes for lithium and lithium-ion batteries. *Lithium Batteries* **2004**, 623-642.

- 30. Kmiec, S.; Joyce, A.; Bayko, D.; Martin, S. W. Glass formation and structure of melt quenched mixed oxy-sulfide Na4P2S7-xOx glasses for $0 \le x \le 5$. *Journal of Non-Crystalline Solids* **2020**, 534, 119776.
- 31. Yao, W.; Martin, S. W. Ionic conductivity of glasses in the MI + M2S + (0.1Ga2S3 + 0.9GeS2) system (M = Li, Na, K and Cs). *Solid State Ionics* **2008**, 178 (33-34), 1777-1784.
- 32. Levasseur, A.; Olazcuaga, R.; Kbala, M.; Zahir, M.; Hagenmuller, P. Synthesis and electrical properties of new sulfide glasses with high ionic conductivity. *C.R.Seances Acad.Sci.*, *Ser.* **1981**, 2, 293, 563-5.
- 33. Mascaraque, N.; Fierro, J. L. G.; Muñoz, F.; Durán, A.; Ito, Y.; Hibi, Y.; Harada, R.; Kato, A.; Hayashi, A.; Tatsumisago, M. Thio-oxynitride phosphate glass electrolytes prepared by mechanical milling. *Journal of Materials Research* **2015**, 30 (19), 2940-2948 DOI: 10.1557/jmr.2015.128.
- 34. Munoz, F.; Duran, A.; Pascual, L.; Montagne, L.; Revel, B.; Rodrigues, A. C. M. Increased electrical conductivity of LiPON glasses produced by ammonolysis. *Solid State Ionics* **2008**, 179 (15-16), 574-579 DOI: 10.1016/j.ssi.2008.04.004.
- 35. Grande, T.; Jacob, S.; Holloway, J. R.; McMillan, P. F.; Angell, C. A. High-pressure synthesis of nitride glasses. *J.Non-Cryst.Solids* **1995**, 184, 151-154.
- 36. Borisov, E. V.; Nifant'ev, E. E. Phosphorus Nitrides. *Russian Chemical Reviews* **1977**, 46 (9), 842-854 DOI: 10.1070/rc1977v046n09abeh002176.
- 37. Day, D. E. Structural role of nitrogen in phosphate glasses. *Journal of Non-Crystalline Solids* **1989**, 112, 7-14.
- 38. Grande, T.; Holloway, J. R.; McMillan, P. F.; Angell, C. A. Nitride glasses obtained by high-pressure synthesis. *Nature* **1994**, 369, 43-45.
- 39. Schnick, W.; Lücke, J.; Krumeich, F. Phosphorus Nitride P3N5: Synthesis, Spectroscopic, and Electron Microscopic Investigations. *Chemistry of Materials* **1996**, 8 (1), 281-286 DOI: 10.1021/cm950385y.
- 40. Vepřek, S.; Iqbal, Z.; Brunner, J.; Schärli, M. Preparation and properties of amorphous phosphorus nitride prepared in a low-pressure plasma. *Philosophical Magazine B* **1981**, 43 (3), 527-547 DOI: 10.1080/01418638108222114.
- 41. Reidmeyer, M. R.; Day, D. E.; Brow, R. K. Phosphorus oxynitride glasses of variable sodium content. *Journal of Non-Crystalline Solids* **1994**, 177 (1313-59-3 (Sodium oxide (Na2O); 1314-56-3 (Phosphorus oxide (P2O5); 7727-37-9 (Nitrogen) Role: PRP (Properties), TEM (Technical or engineered material use), USES (Uses) (glass, sodium nitride phosphate; properties of phosphorus oxynitride glasses of variable sodium content)), 208-215.
- 42. Munoz, F. Kinetic analysis of the substitution of nitrogen for oxygen in phosphate glasses. *Physics and Chemistry of Glasses: European Journal of Glass Science and Technology, Part B* **2011,** 52 (4), 181-186.
- 43. Munoz, F.; Pascual, L.; Duran, A.; Rocherulle, J.; Marchand, R. Oxidation behaviour of Li-Na-Pb-P-O-N oxynitride phosphate glasses. *Journal of the European Ceramic Society* **2006**, 26 (8), 1455-1461 DOI: 10.1016/j.jeurceramsoc.2005.02.019.
- 44. Riguidel, Q.; Munoz, F. Effect of nitridation on the aqueous dissolution of Na2O-K2O-CaO-P2O5 metaphosphate glasses. *Acta Biomaterialia* **2011**, 7 (6), 2631-2636 DOI: 10.1016/j.actbio.2011.03.025.
- 45. Munoz, F. Comments on the structure of LiPON thin-film solid electrolytes. *Journal of Power Sources* **2012**, 198, 432-433 DOI: 10.1016/j.jpowsour.2011.09.009.

- 46. De Souza, J. E.; Rojas De Souza, S.; Gebhardt, R.; Kmiec, S.; Whale, A.; Warthen Martin, S. LiPON and NaPON glasses: A study of the ammonolysis of lithium and sodium metaphosphate melts. *International Journal of Applied Glass Science* **2020**, 11 (1), 78-86.
- 47. Kmiec, S.; Joyce, A.; Martin, S. W. Glass formation and structural analysis of Na4P2S7-xOx, $0 \le x \le 7$ sodium oxy-thiophosphate glasses. *Journal of Non-Crystalline Solids* **2018**, 498, 177-189.
- 48. Baba, T.; Kawamura, Y. Structure and Ionic Conductivity of Li2S–P2S5 Glass Electrolytes Simulated with First-Principles Molecular Dynamics. *Frontiers in Energy Research* **2016**, 4 (22), DOI: 10.3389/fenrg.2016.00022.
- 49. Berbano, S. S.; Seo, I.; Bischoff, C. M.; Schuller, K. E.; Martin, S. W. Formation and structure of Na2S + P2S5 amorphous materials prepared by melt-quenching and mechanical milling. *Journal of Non-Crystalline Solids* **2012**, 358 (1), 93-98 DOI: 10.1016/j.jnoncrysol.2011.08.030.
- 50. Senevirathne, K.; Day, C. S.; Gross, M. D.; Lachgar, A.; Holzwarth, N. A. W. A new crystalline LiPON electrolyte: Synthesis, properties, and electronic structure. *Solid State Ionics* **2013**, 233, 95-101 DOI: https://doi.org/10.1016/j.ssi.2012.12.013.
- 51. Moustafa, Y. M.; El-Egili, K. Infrared spectra of sodium phosphate glasses. *J.Non-Cryst.Solids* **1998**, 240(1-3), 144-153.
- 52. Munoz, F.; Keding, R.; Russel, C.; Marchand, R.; Duran, A.; Pascual, L. Conductivity study of phosphate and oxynitride phosphate glasses in the system Li2O-Na2O-PbO-P2O5. *Phys. Chem. Glasses: Eur. J. Glass Sci. Technol., Part B* **2006,** 47 (1), 58-63.
- 53. Reidmeyer, M. R.; Day, D. E. Structural model for nitrogen incorporation in phosphate glasses. *J.Mater.Res.* **1991,** 6 (8), 1757-1762.
- 54. Redington, W.; Redington, M.; Hampshire, S.; Serantoni, M. Properties of some high Al content glasses in various lanthanide-Si-Al-O-N systems. *Journal of Non-Crystalline Solids* **2003**, 316 (1), 74-81.
- 55. Paine, R. T.; Narula, C. K. Synthetic routes to boron nitride. *Chemical Reviews* **1990**, 90 (1), 73-91 DOI: 10.1021/cr00099a004.
- 56. Peng, Y.; Day, D. E. Factors affecting nitrogen dissolution in sodium metaphosphate glass. *J.Am.Ceram.Soc.* **1987**, 70 (4), 232-236.
- 57. Marchand, R. Nitrogen-containing phosphate glasses. *Journal of Non-Crystalline Solids* **1983,** 56, 173-178.
- 58. Larson, R. W.; Day, D. E. Preparation and characterization of lithium phosphorus oxynitride glass. *Journal of Non-Crystalline Solids* **1986**, 88, 97-113.
- 59. Paraschiv, G. L.; Munoz, F.; Jensen, L. R.; Yue, Y.; Smedskjaer, M. M. Impact of nitridation of metaphosphate glasses on liquid fragility. *Journal of Non-Crystalline Solids* **2016**, 441, 22-28 DOI: 10.1016/j.jnoncrysol.2016.03.009.
- 60. Zheng, Q.; Mauro, J. C. Viscosity of glass-forming systems. *Journal of the American Ceramic Society* **2017**, 100 (1), 6-25 DOI: 10.1111/jace.14678.
- 61. Kmiec, S. J.; Lovi, J. M.; Joyce, A.; Bayko, D.; Martin, S. W. Anomalously strong viscosity behavior in mixed oxy-sulfide Na4P2S7-xOx invert glasses. *Journal of Non-Crystalline Solids* **2021**, 553, 120493 DOI: https://doi.org/10.1016/j.jnoncrysol.2020.120493.
- 62. Strojek, W.; Eckert, H. Medium-range order in sodium phosphate glasses: A quantitative rotational echo double resonance solid state NMR study. *Physical Chemistry Chemical Physics* **2006**, 8 (19), 2276-2285.

- 63. Herms, G.; Sakowski, J.; Gerike, W.; Hoppe, U.; Stachel, D. Short-range and medium-range order in solid and molten metaphosphate glasses. *J.Non-Cryst.Solids* (1998) **1998**, 232-234, 427-433 CODEN: JNCSBJ; ISSN: 0022-3093, 234, 427-234, 433.
- 64. Mascaraque, N.; Durán, A.; Muñoz, F.; Tricot, G. Structural Features of LiPON Glasses Determined by 1D and 2D 31P MAS NMR. *International Journal of Applied Glass Science* **2016,** 7 (1), 69-79 DOI: 10.1111/ijag.12120.
- 65. Peng, Y. B.; Day, D. E. Factors affecting nitrogen dissolution in sodium metaphosphate glass. *J.Am.Ceram.Soc.* **1987**, 70 (4), 232-236.
- 66. Muñoz, F. Kinetic analysis of the substitution of nitrogen for oxygen in phosphate glasses. *Physics and Chemistry of Glasses European Journal of Glass Science and Technology Part B* **2011**, 52 (4), 181-186.

Table of Contents

 $Na_4P_2S_{7-x}O_x$ glasses were melted in an NH_3 atmosphere to incorporate nitrogen into the structure. The N/P ratios were determined from weight loss measurements and CHNS analysis. Reaction mechanisms for N_t and N_d formation in mixed oxy-sulfide glasses were identified with Raman and FTIR spectroscopy. The concentration of available SRO species $(P_2S_7^{4-} \text{ or } PO_3^{-1})$, in close proximity, was found to dictate the maximum solubility of nitrogen.

For Table of Contents Only

